

## THE ISOPHOTAL STRUCTURE OF STAR-FORMING GALAXIES AT $0.5 < z < 1.8$ IN CANDELS: IMPLICATIONS FOR THE EVOLUTION OF GALAXY STRUCTURE

DONGFEI JIANG,<sup>1,2</sup> F. S. LIU <sup>†</sup>,<sup>1,3</sup> XIANZHONG ZHENG,<sup>2,4</sup> HASSEN M. YESUF,<sup>3</sup> DAVID C. KOO,<sup>3</sup> S. M. FABER,<sup>3</sup>  
YICHENG GUO,<sup>5,3</sup> ANTON M. KOEKEMOER,<sup>6</sup> WEICHEN WANG,<sup>7</sup> JEROME J. FANG,<sup>3,8</sup> GUILLERMO BARRO,<sup>3,9</sup> MENG JIA,<sup>1</sup>  
WEI TONG,<sup>1</sup> LU LIU,<sup>1</sup> XIANMIN MENG,<sup>10</sup> DALE KOCEVSKI,<sup>11</sup> ELIZABETH J. MCGRATH,<sup>11</sup> AND NIMISH P. HATHI<sup>12,6</sup>

<sup>1</sup>College of Physical Science and Technology, Shenyang Normal University, Shenyang 110034, China

<sup>2</sup>Purple Mountain Observatory, Chinese Academy of Sciences, 2 West-Beijing Road, Nanjing 210008, China

<sup>3</sup>University of California Observatories and the Department of Astronomy and Astrophysics, University of California, Santa Cruz, CA 95064, USA

<sup>4</sup>Chinese Academy of Sciences South America Center for Astronomy, China-Chile Joint Center for Astronomy, Camino El Observatorio 1515, Las Condes, Santiago, Chile

<sup>5</sup>Department of Physics and Astronomy, University of Missouri, Columbia, MO 65211, USA

<sup>6</sup>Space Telescope Science Institute, 3700 San Martin Drive, Baltimore, MD 21218, USA

<sup>7</sup>Department of Physics & Astronomy, Johns Hopkins University, 3400 N. Charles Street, Baltimore, MD 21218, USA

<sup>8</sup>Astronomy Department, Orange Coast College, Costa Mesa, CA 92626, USA

<sup>9</sup>Department of Astronomy, University of California, Berkeley, CA 94720-3411, USA

<sup>10</sup>National Astronomical Observatories, Chinese Academy of Sciences, A20 Datun Road, Beijing 100012, China

<sup>11</sup>Department of Physics and Astronomy, Colby College, Mayflower Hill Drive, Waterville, ME 0490, USA

<sup>12</sup>Aix Marseille Université, CNRS, LAM (Laboratoire d'Astrophysique de Marseille) UMR 7326, 13388, Marseille, France

### ABSTRACT

We have measured the radial profiles of isophotal ellipticity ( $\varepsilon$ ) and disk/boxy parameter  $A_4$  out to radii of about three times the semi-major axes for  $\sim 4,600$  star-forming galaxies (SFGs) at intermediate redshifts  $0.5 < z < 1.8$  in the CANDELS/GOODS-S and UDS fields. Based on the average size versus stellar-mass relation in each redshift bin, we divide our galaxies into *Small* SFGs (SSFGs), i.e., smaller than average for its mass, and *Large* SFGs (LSFGs), i.e., larger than average. We find that, at low masses ( $M_* < 10^{10} M_\odot$ ), the SSFGs generally have nearly flat  $\varepsilon$  and  $A_4$  profiles for both edge-on and face-on views, especially at redshifts  $z > 1$ . Moreover, the median  $A_4$  values at all radii are almost zero. In contrast, the highly-inclined, low-mass LSFGs in the same mass-redshift bins generally have monotonically increasing  $\varepsilon$  with radius and are dominated by disk-like values at intermediate radii. These findings at intermediate redshifts imply that low-mass SSFGs are not disk-like, while low-mass LSFGs appear to harbour disk-like components flattened by significant rotation. At high masses ( $M_* > 10^{10} M_\odot$ ), highly-inclined SSFGs and LSFGs both exhibit a general, distinct trend for both  $\varepsilon$  and  $A_4$  profiles: increasing values with radius at lower radii, reaching maxima at intermediate radii, and then decreasing values at larger radii. Such a trend is more prevalent for more massive ( $M_* > 10^{10.5} M_\odot$ ) galaxies or those at lower redshifts ( $z < 1.4$ ). The distinct trend in  $\varepsilon$  and  $A_4$  can be simply explained if galaxies possess all three components: central bulges, disks in the intermediate regions, and halo-like stellar components in the outskirts.

*Keywords:* galaxies: photometry — galaxies: star formation — galaxies: high-redshift

## 1. INTRODUCTION

In the  $\Lambda$ CDM framework of hierarchical growth of structures, galaxies are assembled by mergers and low-mass accretion events (e.g. Eggen et al. 1962; Sandage 1986; Purcell et al. 2007; Johnston et al. 2008; De Lucia & Helmi 2008; Cooper et al. 2013; Pillepich et al. 2014). While disk galaxies can be formed in the centers of dark-matter halos via gas infall, elliptical galaxies and bulges, which we refer to as spheroids, form via violent major mergers (e.g. Kauffmann et al. 1993; Baugh et al. 1996). Stars stripped from infalling satellite galaxies form a diffuse and highly-structured stellar halo surrounding the central galaxy. As a consequence of the relatively-long, dynamical timescales in the outskirts of galaxies, such halos retain a “memory” of past accretion events (e.g. Eggen et al. 1962; Searle & Zinn 1978; Steinmetz & Muller 1995; Bekki & Chiba 2001; Samland & Gerhard 2003).

The past decade has experienced major advances in our understanding of the formation and evolution of bulges (see Tonini et al. 2016a,b, for reviews). Bulges are now divided into two main types: classical bulges and pseudo-bulges (Kormendy 1993; Kormendy & Kennicutt 2004). Classical bulges resemble elliptical galaxies by being dynamically-hot spheroids with stellar motions dominated by velocity dispersion rather than rotation; they usually have a strongly-concentrated structure (e.g., Sérsic index  $n \sim 4$ ). The pseudo-bulges are dynamically colder and exhibit characteristics (e.g., in Sérsic indices and velocity dispersions) between classical bulges and flattened (oblate) disks. Another common feature of pseudo-bulges is their disky shape, which spurred Kormendy & Illingworth (1982) to suggest that secular processes are responsible for their formation.

One path to improve our understanding of the formation of the two bulge types would be to quantify the relative importance of different channels of galaxy evolution, such as merger-driven versus secular processes (Kormendy & Kennicutt 2004). Recently, instabilities in disks (e.g., Krumholz & Burkert 2010; Bournaud et al. 2011; Forbes et al. 2012; Cacciato et al. 2012) and mass transfer from unstable disks have been proposed as effective mechanisms to form bulges within disk galaxies at high redshifts (e.g., Noguchi 1999; Elmegreen et al. 2008; Dekel et al. 2009; Hathi et al. 2009; Genzel et al. 2011; Forbes et al. 2014). Even more recently, Tonini et al. (2016a) proposed two distinct populations of bulges: merger-driven bulges, akin to classical bulges, and instability-driven bulges, akin to pseudo-bulges. Huertas-Company et al. (2015) also proposed two distinct channels for the growth of bulges in massive galaxies. One channel formed around one third (1/3) of

the bulges at early epochs (before  $z \sim 2.5$ ) through gas-rich mergers or violent disk instabilities – these usually have high Sérsic indices ( $n > 3 - 4$ ) and small effective-radii ( $\sim 1$  kpc). The remaining two thirds (2/3) underwent a gradual transformation in morphology at late epochs, from clumpy disks to more-regular, bulge+disk systems. Such changes result in significant growth of bulges with low Sérsic indices ( $n < 3$ ). If such secular evolution is a more important process in forming the bulge population at late epochs, bulges should be observed to grow in parallel with disk growth.

Besides having a disk and bulge, fairly-large and massive spiral galaxies, such as the Milky Way (MW), often also have extended stellar halos. The stellar halo of the Milky Way has been well-characterized (see a review by Helmi 2008). Recent observational advances have also enabled the detection of faint stellar halos around external galaxies, such as M31 (Ferguson et al. 2002; Guhathakurta et al. 2005; Irwin et al. 2005; Ibata et al. 2007) and other nearby disk galaxies (Mouhcine et al. 2005a,b; de Jong et al. 2007; Ibata et al. 2009; Mouhcine et al. 2010). The observed properties of the stellar halos in the Milky Way and its neighbouring galaxies are in general agreement with the predictions of  $\Lambda$ CDM hierarchical galaxy formation models (Bell et al. 2008; Gilbert et al. 2009; McConnachie et al. 2009; Starkenburg et al. 2009; Martínez-Delgado et al. 2010). Cosmological simulations predict that the amount of stellar mass in these halos should be  $\sim 10^8 - 10^9 M_\odot$  for MW-like galaxies, and that most of the stellar halo mass would be assembled before  $z \sim 1$  (De Lucia & Helmi 2008; Cooper et al. 2010; De Lucia 2012, for a review)

The detection of stellar halos in distant disk galaxies has, however, been scarce, thereby stemming progress in tracking the early formation and assembly histories of disk galaxies. Only two works have detected stellar halos beyond  $z = 0.3$  (Zibetti & Ferguson 2004; Trujillo & Bakos 2013). Exploiting deep, high-resolution *HST* images in the *Hubble Ultra Deep Field* (HUDF; Beckwith et al. 2006). Zibetti & Ferguson (2004) detected the stellar halo of a disk galaxy at  $z = 0.32$  and Trujillo & Bakos (2013) detected the stellar halos of two MW-like galaxies at  $z \sim 1$ . Thanks to the large sample of galaxies with HST imaging in the Cosmic Assembly Near-Infrared Deep Extragalactic Legacy Survey (CANDELS, Grogin et al. 2011; Koekemoer et al. 2011), we can now detect and study the stellar halos at intermediate to high redshifts in a statistical manner, and significantly advance our understanding of the assembly histories of disk galaxies.

In local galaxies, the isophotal shapes of galaxies are found to be coupled with their structural and kinematic

properties. The isophotes of spheroids often deviate from pure ellipses. These deviations originate from the characteristics of the stellar orbits that make up these galaxies. The correlations between the isophotal deviations and physical properties of galaxies were shown mostly for nearby early-type galaxies (e.g. Carter 1978; Lauer 1985; Bender et al. 1988, 1989; Hao et al. 2006) and for a few late-type galaxies (e.g. Erwin & Debattista 2013).

Besides isophotal deviations, the ellipticity (1 - axis ratio) of a galaxy has been shown to be closely linked with the relative importance of ordered rotation and random motion in spheroids (Kormendy 2013). Furthermore, the ellipticity is linked to the isophotal deviations themselves (Hao et al. 2006). Generally, more flattened systems (with larger ellipticities) tend to be more rotationally supported and have more disk-like isophotal shapes. Therefore, measurements of radial profiles of isophotal ellipticity and deviations are likely to be helpful diagnostics of the kinematics and morphological compositions of galaxies. For example, disk galaxies seen nearly edge-on appear flattened and have more disk-like isophotal shapes than galaxies dominated by central bulges or outer stellar halos (Zheng et al. 2015).

Furthermore, quantifying the variation of isophotal shape profiles across cosmic time may provide key insights on the evolution of galaxy structure. With this motivation, we used the deep, high-resolution *HST*/WFC3 imaging data to measure the radial profiles of isophotal ellipticity ( $\varepsilon$ ) and deviation parameter  $A_4$  (defined in §3) for  $\sim 4,600$  *UVJ*-defined SFGs at  $0.5 < z < 1.8$  selected from the CANDELS/GOODS-S and UDS fields. The isophotal-shape profiles are well measured to large radii of about three times the semi-major axes for more than 2/3 of the galaxies in our sample. For the first time, statistically-robust profile analyses of the isophotal shapes out to large radii in distant star-forming galaxies is possible. We study the stacked (median)  $\varepsilon$  and  $A_4$  profiles of our galaxies subdivided by stellar mass and redshift. We also divide our galaxies into *Small* and *Large* SFGs which are smaller and larger than the average size-mass relation, respectively. The two classes of SFGs are found to exhibit statistically significant differences in their radial profiles of the isophotal shape parameters.

The outline of this paper is as follows. Section 2 describes the data and the sample selection. Sections 3 details the measurements of isophotal shape profiles. We present our main results in Section 4 and finish with a discussion and summary in Section 5. Throughout the paper, we adopt a cosmology with  $\Omega_M=0.3$ ,  $\Omega_\Lambda=0.7$  and

$H = 70 \text{ km s}^{-1} \text{ Mpc}^{-1}$ . All magnitudes are in the AB system.

## 2. DATA AND SAMPLE SELECTION

### 2.1. Data

The sample of galaxies used in this work is selected from the CANDELS/GOODS-S and UDS fields (Grogin et al. 2011; Koekemoer et al. 2011). Multi-wavelength photometry catalogs of the two publicly-available fields were built by Guo et al. (2013, for GOODS-S) and Galametz et al. (2013, for UDS); they provide details on source identification and photometry. Key points for both fields include source detection from the CANDELS mosaics in the F160W band with total fluxes of the sources in the *HST* bands being measured by running **SExtractor** (Bertin & Arnouts 1996) in dual mode on the point spread function (PSF)-matched images. Photometry in the lower-resolution images (e.g., ground-based and IRAC) was measured using **TFIT** (Laidler et al. 2007).

Redshifts used in this study are spectroscopic, if available, and are otherwise photometric redshifts. Photometric redshifts were computed using the official multi-wavelength photometry catalogs described above and adopting a hierarchical Bayesian approach. The typical scatter of photometric redshifts spans from 0.03 to 0.06 in  $z$  (see Dahlen et al. 2013, for details). To compute rest-frame total magnitudes from FUV to  $K$  band, the redshifts are input to the **EAZY** software package (Brammer et al. 2008), which fits a set of galaxy spectral energy distribution (SED) templates to the multi-wavelength photometry. For stellar masses, we adopt the CANDELS official values released by Santini et al. (2015), which are the median of ten separate SED fitting results (Mobasher et al. 2015) after being scaled to the Chabrier (2003) initial mass function (IMF). The typical formal uncertainty of stellar masses is  $\sim 0.1$  dex (see Santini et al. 2015, for details).

Spatially-resolved photometry is taken from the *HST*-based multi-band and multi-aperture photometry catalogs of CANDELS still under construction by Liu et al. (in preparation). These catalogs include the radial profiles of isophotal ellipticity ( $\varepsilon$ ) and disk/boxy parameter  $A_4$  in both F125W(J) and F160W(H), and the observed surface brightness profiles in all *HST*/WFC3 and ACS bands if available. The detailed procedure of isophotal measurement is presented in §3.

Global-galaxy structural parameters measured by van der Wel et al. (2012) with **GALFIT** (Peng et al. 2002) are available for all galaxies in two fields. Images of each galaxy in both F125W and F160W were fit with a single-Sérsic model, yielding the best-fitting Sérsic index

( $n$ ), effective radius along the semi-major axis ( $R_{\text{SMA}}$ ), axis ratio ( $b/a$ ), and position angle (PA), along with estimates of their errors. We use  $R_{\text{SMA}}$  as our indicator of galaxy size, rather than circularized effective radius,  $R_{\text{eff}}$ , because the latter depends on the axis ratio ( $R_{\text{eff}} \equiv \sqrt{b/a} \times R_{\text{SMA}}$ ), and  $R_{\text{SMA}}$  is a more faithful indicator of the intrinsic size for oblate systems.

## 2.2. Sample Selection

The full GOODS-S and UDS catalogs contain 34,930 (Guo et al. 2013) and 35,932 (Galametz et al. 2013) objects, respectively. The parent sample used in our analysis is constructed by applying the following criteria to the catalogs:

1. Observed F160W(H) magnitude brighter than 24.5 and the GALFIT quality flag = 0 in F125W for  $z < 1$  and F160W for  $z > 1$  (van der Wel et al. 2012) to ensure well-constrained GALFIT measurements and to eliminate doubles, mergers, and disturbed objects. Table 1 shows that only about a quarter of galaxies in the combined sample of GOODS-S and UDS satisfy this criterion.

2. SExtractor Photometry quality flag PhotFlag = 0 to exclude spurious sources;

3. SExtractor CLASS\_STAR < 0.9 to reduce contamination by stars;

4. Redshifts between  $0.5 < z < 1.8$  and stellar masses of  $9.0 < \log M_*/M_\odot < 11.0$  to maintain a high mass-completeness limit for SFGs ( $\sim 100\%$  at  $z = 0.5$  and  $\sim 85\%$  at  $z = 1.8$ ) (van der Wel et al. 2014a) and to assure that all isophotal parameters can be measured in similar, rest-frame optical bands.

5. Well-constrained measurements of isophotal parameters (Isophotal PhotFlag = 0) from Liu et al. (in preparation);

6.  $R_{\text{SMA}} > 0.18''$  (3 drizzled pixels) to reduce the effect of PSF smearing on isophotal measurements;

7. SFGs are selected from rest-frame  $UVJ$  diagrams by  $((U - V) < 0.88 \times (V - J) + 0.49$  for  $z > 1$  and  $(U - V) < 0.88 \times (V - J) + 0.59$  for  $z < 1$ ) following the criteria defined by Williams et al. (2009);

8. Exclude a few compact SFGs (cSFGs) with the criterion of  $\log \Sigma_{1.5} > 10.3$  from Barro et al. (2013), since these cSFGs might start as compact quiescent galaxies at high redshifts and later evolve into larger quiescent

galaxies at lower redshifts (e.g., Barro et al. 2013, 2017).

After the above cuts, 4,595 SFGs remain: 2,033 from GOODS-S and 2,562 from UDS. Table 1 lists the resulting sample size after applying each selection criterion. The top panels of Figure 1 present the rest-frame  $UVJ$  diagrams for our galaxies in three redshift bins. SFGs defined by the criteria of Williams et al. (2009) are shown with blue dots and color-coded by  $\log R_{\text{SMA}}$ . Quiescent galaxies are excluded in this work and they are located in the gray hatched upper corners of the diagrams. The bottom panels of Figure 1 show the size( $\log R_{\text{SMA}}$ )-mass relations for  $UVJ$ -defined SFGs in the three adopted redshift bins. The size-mass panels are color-coded by the global ellipticity defined as  $\varepsilon_{\text{global}} = 1 - (b/a)_{\text{Galfit}}$ . To derive the mean size-mass relations, an initial fit to all SFGs is made; objects more than  $2\sigma$  away from the fit are then excluded for the next fit. This fitting process is repeated until no new objects are excluded. The parameters of the final fits are presented in Table 2. The solid black lines in the bottom panels of Figure 1 indicate the adopted best-fit linear relations to the galaxies. After the fits are done, vertical offsets in  $\log R_{\text{SMA}}$  from the relations are calculated for our SFGs in each bin. The offset for a given galaxy is denoted by  $\Delta \log R_{\text{SMA}}$ . For simplicity, we hereafter refer to galaxies (in a given mass and redshift bin) with  $\Delta \log R_{\text{SMA}} > 0$  (i.e., larger than average) as *Large* SFGs (LSFGs), and galaxies with  $\Delta \log R_{\text{SMA}} < 0$  as *Small* SFGs (SSFGs). Note that our slopes are systematically shallower by  $\sim 0.1$  dex compared to the fits by van der Wel et al. (2014a), probably due to the exclusion of very small galaxies with  $R_{\text{SMA}} < 0.18''$ . These small discrepancies do not affect our results, since we are only concerned with relative-size differences at fixed mass and redshift.

To examine evolutionary trends as a function of both redshift and mass at the same time, we divide the sample into four mass bins ( $9.0 < \log M_* < 9.5$ ,  $9.5 \leq \log M_* < 10.0$ ,  $10.0 \leq \log M_* < 10.5$  and  $10.5 \leq \log M_* < 11.0$ ) and three redshift bins ( $0.5 < z < 1.0$ ,  $1.0 < z < 1.4$ , and  $1.4 < z < 1.8$ ). This 4x3 grid of diagrams is a powerful visualization tool to track the movement of galaxies as they evolve in mass with time. Figure 2 shows the distributions of  $\varepsilon_{\text{global}}$  and corresponding median values ( $\varepsilon_{\text{global,med}}$ ) for SSFGs and LSFGs in each mass-redshift bin, respectively. To recognize the intrinsic structure of galaxies more easily, we further divide our sample galaxies into two sub-classes: “edge-on” ( $\varepsilon_{\text{global}} > \varepsilon_{\text{global,med}}$ ) and “face-on” ( $\varepsilon_{\text{global}} < \varepsilon_{\text{global,med}}$ ), according to the relative observed “inclination”. So that our isophotal analyses are done in similar rest-frame optical bands,



we measure the isophotal profiles in F160W band for  $z > 1$  galaxies and in F125W band for  $z < 1$  galaxies.

### 3. MEASUREMENT OF ISOPHOTAL SHAPE PROFILES

The radial profiles of galaxy isophotal parameters,  $\varepsilon$  and  $A_4$ , used in this work come from the *HST*-based, multi-wavelength and multi-aperture photometry catalogs built by Liu et al. (in preparation). The isophotal parameters are measured by using the IRAF routine `ellipse` within STSDAS, which is based on a technique described by Jedrzejewski (1987). We now summarize the measurement process.

First, we trim the original PSF-matched mosaic images in each band to generate multi-band cut-out images centered on each target galaxy. Before the ellipse fitting, SExtractor is used to identify sources within the detection limit; they are removed then to obtain a background-only image for each band. Median filtering is applied to derive a local-background image in each band, using sigma clipping to reduce the impact of relatively-brighter, residual background-sources. This local background is then subtracted from each cut-out image. We verify that the flux distributions in empty regions of each cut-out image in each band are centered on zero after the background subtraction.

After background subtraction, we run SExtractor again on the trimmed image to generate a ‘SEGMENTATION’ image, which identifies all objects with flags in the image. A mask image, with all the detected objects flagged except the galaxy of interest, is then obtained from the ‘SEGMENTATION’ image. We carefully examine all the mask images in each band and correct a few bad images manually to create good mask images for all galaxies. Photometry is then performed on the trimmed images with the masked areas excluded from the reduction.

We use the geometric center, ellipticity, position angle and effective radius along the semi-major axis of sample galaxies obtained from the GALFIT measurements by van der Wel et al. (2012) as initial values in the ellipse fitting. In the `ellipse` task, the image intensity is first sampled along a trial ellipse generated using these parameters, and the intensity string  $I(\theta)$  is expanded in a Fourier series,

$$I(\theta) = I_0 + \sum_{n=1}^N [A_n \cos(n\theta) + B_n \sin(n\theta)] \quad (1)$$

where  $I(\theta)$  is the intensity (in units of  $\text{ADU s}^{-1} \text{ pixel}^{-1}$ ) on the ellipse in the direction of  $\theta$ ,  $I_0$  is the average intensity of the ellipse, the position angle  $\theta$  is defined to be  $0^\circ$  along the positive  $y$ -axis and increases counter

clockwise.  $N$  is the highest harmonic fitted,  $A_n$  and  $B_n$  are the Fourier coefficients. The most significant non-zero component of the Fourier analysis is the  $A_4$  parameter (corresponding to the  $\cos(4\theta)$  term). Using the sign of this parameter, the isophote of a galaxy is classified as disk ( $A_4 > 0$ ) or boxy ( $A_4 < 0$ ).

During the fitting, we allow the geometric center, ellipticity and position angle to vary freely. Successive ellipses are fitted along the major axis, starting from the effective radius and moving inward and outward with logarithmic steps of 0.3, until the ellipse fitting process fails to converge. The output of `ellipse` is a table containing the radial profiles of several isophotal parameters (along with their uncertainties), such as ellipticity ( $\varepsilon$ ), Fourier coefficients (i.e.,  $A_4$ ), position angle (PA), and surface brightness in each elliptical annulus. Figure 3 illustrates our measurements for three nearly edge-on galaxies (GOODS-S 14994, GOODS-S 22208 and GOODS-S 19762) and Figure 4 for three nearly face-on galaxies (GOODS-S 10421, GOODS-S 26255 and UDS12524) in three different redshift bins.

We stress the importance of two steps in the above process: the local background subtraction and the use of large logarithmic steps. Both significantly improve the accuracy of the measurements. More technical details will be included in the documentation of the Liu et al. (in preparation) catalogs.

### 4. RESULTS

To derive the stacked  $\varepsilon$  and  $A_4$  profiles for each subclass in every mass-redshift bin, we adopt IRAF/`proto` to do cubic spline interpolation and then compute the median value and 68% distribution of the scatter for every selected position in each bin. The resulting median  $\varepsilon$  and  $A_4$  as a function of normalized radius ( $\bar{R} = R/R_{\text{SMA}}$ ) for SSFGs and LSFGs are shown in Figures 5 to 8. Note that not every galaxy has a reliable measurement of isophotal profile that extends to large radii. The median values at the positions where the fractions of accurate data points are below  $1\sigma$  are removed in our analysis.

To quantify the general trends of composite  $\varepsilon$  and  $A_4$  profiles in each mass-redshift bin, we use the `segmented` package in R programming language to fit the two-broken-lines model to each profile outside the PSF FWHM ( $0.18''$ ). The model is derived simultaneously yielding point estimates and their approximate standard errors for all the model parameters, including the break-point where the linear relation changes. If the two broken lines model fails to fit a profile, the program automatically generates a single linear regression model. The best-fit parameters are given in Table 3, including the slopes, intercepts, relevant standard errors,

break-radii, and R-squared values. The R-squared value quantifies how well the model fits the data. R-squared values close to 1 indicate excellent fits while those close to zero indicate poor fits. Table 3 shows that the majority of segmented models are good enough to trace the trends of our profiles. The best models with  $2\sigma$  lower and upper limits are shown shaded in Figures 5 to 8.

Next, we summarize the observed trends of  $\varepsilon$  and  $A_4$  profiles with mass and viewing angle. First, we discuss the trends observed in low-mass galaxies before those in high-mass galaxies.

1. At low masses ( $M_* < 10^{10}M_\odot$ ), the SSFGs ( $\Delta\log R_{\text{SMA}} < 0$ ) generally have nearly flat  $\varepsilon$  profiles (the majority of segmented models have slope values within  $\pm 0.2$  of zero) in both face-on and edge-on views, especially at  $z > 1$  (Figure 5). The average ellipticity values are  $\sim 0.4$  for edge-on and  $\sim 0.2$  for face-on, which imply that these systems are not intrinsically highly flattened. The flat  $\varepsilon$  profiles in face-on views are generally consistent with our expectations and, therefore, are not surprising. In contrast, if these galaxies actually harbor disks and are being viewed edge-on, a significant change in  $\varepsilon$  with increasing radius should be observed (Zheng et al. 2015). Such trends, however, are not observed in edge-on views. These findings indicate that these galaxies are likely composed of a single structure and it is not disk-like. In addition, we find that the SSFGs in these bins also have nearly flat  $A_4$  profiles (the slopes of segmented models are within  $\pm 0.02$  of zero) in both face-on and edge-on (Figure 6); furthermore, the median values of  $A_4$  at all radii are almost zero. These findings imply that, statistically, these galaxies are not rotationally supported and, thus, they are not disks. These systems may not be spheroidal either, because they usually have Sérsic indices  $n \sim 1$  (Wuyts et al. 2011). Hao et al. (2006) showed the relation between  $\varepsilon$  and  $A_4$  for nearby massive spheroids and find that spheroidal systems with  $\varepsilon = 0.4$  are usually disk ( $A_4 > 0$ ). If this relation were to hold for low-mass systems at higher redshifts, it would provide another argument against our observed sample being spheroids. Furthermore, it can be seen in Figure 6 that the  $A_4$  points of these galaxies distribute on both sides of the  $A_4 = 0$  lines randomly, and the face-on and edge-on systems are mixed together. The findings suggest that these galaxies are likely to have irregular structures without distinct boundaries of regular components.

Likewise, the low-mass ( $M_* < 10^{10}M_\odot$ ) LSFGs ( $\Delta\log R_{\text{SMA}} > 0$ ) in the same bins also have relatively flat  $\varepsilon$  profiles in face-on views (Figure 7). When seen in edge-on, however, these large systems have  $\varepsilon$  profiles that mainly increase monotonically with radius (the

slopes of inner fits are greater than  $\sim 0.2$ ). Although some LSFGs have decreasing  $\varepsilon$  profiles in their outermost regions, these trends are relatively weak compared to those observed in high-mass galaxies.

For the low-mass LSFGs, the average ellipticity values are  $\sim 0.55$  for edge-on views and  $\sim 0.35$  for face-on views. This result implies that these systems are more flattened intrinsically than the SSFGs in the same mass-redshift bins. The low-mass LSFGs exhibit more positive  $A_4$  (disky) profiles that dominate in the intermediate regions when seen edge-on than face-on (Figure 8). This finding implies that these large galaxies likely have disk-like components flattened by rotation.

2. At high masses ( $M_* > 10^{10}M_\odot$ ), the SSFGs also have nearly flat  $\varepsilon$  profiles in face-on views (Figure 5). In edge-on views, however, the  $\varepsilon$  profiles of SSFGs exhibit a distinctly different pattern compared to those for low-mass SSFGs: significant increase with radius in the inner regions (the slopes are greater than 0.2); goes through a maximum at intermediate radii; followed by decrease in the outskirts (the slopes become negative). Such trends are more prevalent for more massive ( $M_* > 10^{10.5}M_\odot$ ) galaxies or at lower redshifts ( $z < 1.4$ ) and especially clear for the LSFGs (see Figure 7). Even for face-on views, similar trends are seen for the most massive ( $M_* > 10^{10.5}M_\odot$ ) LSFGs. The trend is likely due to the presence of three components: bulges in the inner regions, disks in the intermediate regions, and halo-like stellar components in the outskirts. When viewed edge-on, galaxies should exhibit ellipticity profiles that reveal the relative flattening of various components. The central bulge and outer stellar halo will appear much rounder than the disk in the intermediate region. Similar trends can be found in the corresponding  $A_4$  profiles of edge-on systems (Figures 6 and 8): the isophotes in the intermediate regions are obviously disk-like with positive  $A_4$ , whereas the inner and outer isophotes are close to perfect ellipses ( $A_4 \sim 0$ ). Furthermore, compared to the low-mass ( $M_* < 10^{10}M_\odot$ ) galaxies at the same redshifts, the intermediate regions of high-mass galaxies are more disk-like (with larger  $A_4$  values) in edge-on views. This result implies that these massive galaxies likely possess disks with relatively faster rotation.

To clearly trace the variation of ellipticities in the inner regions as galaxies evolve in mass with time, we present in Figure 9 the distributions of ellipticity at  $R = 1.5\text{kpc}$  ( $\varepsilon_{1.5}$ ) for the SSFGs and LSFGs in each mass-redshift bin. This physical radius ( $R = 1.5\text{kpc}$ ) is relatively close to the centers of galaxies but the ellipticity measurement at this radius is less affected by PSF smoothing compared to the very center at  $R_{\text{SMA}} < 0.18''$ , as indicated in Figures 5 and 7. One sees that,

as galaxies evolve towards high stellar masses and low redshifts, the  $\varepsilon_{1.5}$  of both SSFGs and LSSFGs tend to decrease (become rounder) statistically.

To double-check our results, we visually inspect the images of sample galaxies carefully. In Figure 10, we present cut-out images of 4 examples of highly-inclined systems for different mass-redshift bins. In each panel, the upper two images are for LSFs and the lower two are for SSFGs. Obviously, in the low-mass ( $M_* < 10^{10} M_\odot$ ) and high-redshift ( $z > 1$ ) bins, the images of SSFGs exhibit good consistency with no obvious disk-like features (mostly irregular morphology). In contrast, the images of LSFs in the same bins indeed exhibit possible disk-like structure. As galaxies evolve towards the high masses ( $M_* > \sim 10^{10} M_\odot$ ) and low redshifts ( $z < \sim 1.4$ ), the disk component becomes more prominent in both LSFs and SSFGs. Meanwhile, the diffuse, halo-like stellar components appear to dominate the outer regions of galaxies. The visual inspection is in good agreement with our quantitative analysis of the isophotal structure.

## 5. DISCUSSION AND SUMMARY

We have measured the radial profiles of isophotal ellipticity ( $\varepsilon$ ) and  $A_4$  out to radii of  $\sim 3R_{\text{SMA}}$  in similar, rest-frame, optical bands for  $\sim 4,600$  SFGs between redshift 0.5 and 1.8 in the CANDELS/GOODS-S and UDS fields. With this sample, we study the stacked  $\varepsilon$  and  $A_4$  profiles on an evolutionary grid laid out by stellar mass and redshift (see Figure 6 in Fang et al. 2017). The grid of sub-panels is a useful visualization tool to track the movement of galaxies as they evolve in stellar mass (Moster et al. 2013; Papovich et al. 2015). For the first time, we are able to undertake a statistically robust analysis of the isophotal structure of distant star-forming galaxies. The mean size-mass relation in a given redshift bin is used as the divider between the relatively *Small* SFGs (SSFGs) and *Large* SFGs (LSFGs). We find that, statistically, these two classes exhibit different radial patterns of isophotal shape. Our main conclusions are as follows:

1. At low masses ( $M_* < 10^{10} M_\odot$ ), the SSFGs generally have nearly flat  $\varepsilon$  and  $A_4$  profiles in both edge-on and face-on views, especially at  $z > 1$ . Moreover, the median  $A_4$  values at all radii are almost zero with no disk-like or boxy signatures, but the  $A_4$  distributions have quite large scatter. In contrast, the more-inclined (edge-on) LSFs in the same mass-redshift bins generally have  $\varepsilon$  profiles that mainly increase monotonically with radius and disk-like profiles ( $A_4 > 0$ ) that dominate in the intermediate regions. The findings imply that SSFGs

are not disk-like, whereas LSFs likely have disk-like components flattened by significant rotation.

2. At high masses ( $M_* > 10^{10} M_\odot$ ), both more-inclined SSFGs and LSFs generally exhibit distinct  $\varepsilon$  and  $A_4$  profiles that first increase with radius, then reach maxima, and finally decrease. Such trends are more prevalent at lower redshifts ( $z < 1.4$ ) or for more massive ( $M_* > 10^{10.5} M_\odot$ ) galaxies. This profile pattern can be explained by the galaxies possessing central bulges, disks in the intermediate region, and halo-like stellar components in the outskirts. Compared to the low-mass SFGs at the same redshifts, the intermediate isophotes of edge-on massive SFGs are more disk-like, indicating that these massive galaxies likely have disks with faster rotation.

3. Central ellipticities of both SSFGs and LSFs tend to decrease (become rounder) with increasing mass and decreasing redshift. Moreover, the peak values of both ellipticity and  $A_4$  tend to increase as galaxies increase in mass with time. These findings suggest bulges enlarge with disk growth.

Recently, van der Wel et al. (2014b) derived the intrinsic, 3-dimensional distributions of global axis ratio ( $b/a = 1 - \varepsilon$ ) of distant SFGs through the observed ellipticity distribution. They showed that the low-mass ( $M_* < 10^{10} M_\odot$ ) SFGs at  $z > 1$  possess a broad range of geometric shapes, and the fraction of non-disk (probably prolate) galaxies increases at higher redshifts and lower masses. This result is consistent with our finding. More recently, Liu et al. (2016) showed that the rest-frame *NUV-B* color gradients in low-mass ( $M_* < 10^{10} M_\odot$ ) SFGs at  $z \sim 1$  are generally flat after correcting for dust reddening, which implies that the newly-formed stars in these galaxies may be randomly mixed with older populations. These galaxies may be supported predominantly by random motions, a result also consistent with our  $A_4$  analysis. Recent cosmological hydrodynamical zoom-in simulations by Ceverino et al. (2014) show that low-mass galaxies at high redshifts are sometimes elongated, bar-like systems with irregular morphology. The large and homogeneous survey with integral field spectroscopy (IFS) by KMOS (e.g., Wisnioski et al. 2015) reveals that  $\sim 83\%$  of SFGs with  $M_* = 3 \times 10^9 - 7 \times 10^{11} M_\odot$  at  $0.7 < z < 2.7$  are rotation dominated and  $\sim 70\%$  of SFGs are disk-like systems. Galaxies that are resolved by KMOS, but not rotating, are found primarily at low stellar masses. These findings are also qualitatively consistent with our isophotal analyses.

We caution that whether the change in the ellipticity is observed for single-component rotating disks is unclear. Also, the relation between positive  $A_4$  and fast rota-

tion is seen only in nearby early-type galaxies (e.g., Hao et al. 2006). Whether single-component disk galaxies tend to have positive  $A_4$  values is also not clear. We interpret the increasing inner and decreasing outer profiles of ellipticity and  $A_4$  as the consequence of galaxies having multiple components of inner bulges, intermediate-scale disks, and outer stellar halos. It should be sobering that star-forming galaxies often also have additional substructures, such as spiral arms, rings, clumps, and bars (e.g. Erwin & Sparke 2002; Guo et al. 2015; Cheung et al. 2013). The spiral arms, clumps, and rings tend to appear randomly and they may not affect our profiles once they are mixed in our stacks, whereas bars could have significant effects on our results (e.g. Erwin & Debattista 2013).

We show the distributions of Sérsic index ( $n$ ) of our sample galaxies in the same mass-redshift grid in Figure 11. Both LSFs and SSFGs exhibit increasing Sérsic indices as galaxies evolve towards the high masses and low redshifts. This trend indicates that the fraction of bulge-dominated systems likely increases as galaxies evolve, a result in agreement with previous studies (e.g. van der Wel et al. 2011; Bruce et al. 2012; Huertas-Company et al. 2015; Margalef-Bentabol et al. 2016; Barro et al. 2017). Note that Sérsic indices here are not those of bulges but, instead, are those of the entire galaxy. Investigations of bulge Sérsic indices will be possible with the advent of improved spatial resolution and higher S/N provided by *JWST*.

What leads to decreasing ellipticities in the outskirts of the highly-inclined massive galaxies is quite intriguing. Based on our isophotal analyses and visual inspections of images, we propose halo-like stellar components in the outer region. Zheng et al. (2015) showed that the composite ellipticity profile of nearby disk galaxies rises slowly between  $\sim 0.5R_{90}$  and  $\sim 1.4R_{90}$  and then slowly declines out to  $\sim 3R_{90}$  (see Figure 11 in their paper). For a pure disk galaxy having an exponential radial surface brightness profile,  $R_{90}$  is roughly twice the effective radius. The transition radii in the ellipticity profiles of our massive SFGs are roughly between  $R_{\text{SMA}}$  and  $2R_{\text{SMA}}$ , which are slightly smaller than, but already comparable to, that of local disk galaxies reported by Zheng et al. (2015). We also show that the

outer ellipticity and  $A_4$  beyond  $2R_{\text{SMA}}$ , seem to be constant over time, which might favor scenarios that have halo-like stellar components already existing at high redshifts (i.e.,  $z \sim 2$ ). Our finding should be regarded with caution, since cosmological surface-brightness dimming makes observations of faint stellar halos at high redshifts extremely difficult. Zheng et al. (2015) further showed that the characteristic radial profiles of color, stellar mass-to-luminosity ratio ( $M/L$ ), and stellar age of nearby disk galaxies have a “U” shape (they first decline with increasing radius, but then rise in the outer region). The minima are also located at radii of around 0.8 to 1.0  $R_{90}$  or at locations where the local stellar mass surface density is  $\sim 10M_{\odot}/\text{pc}^{-2}$ . These findings further support the contribution of halo light beyond such radii. With these observational results, Zheng et al. (2015) argued that a combination of a radial migration of stars in the inner region and a truncation of recent star formation in the outer part is likely to be required to regulate the evolution of disk galaxies. The general trend for nearby disk galaxies to have redder (older) outer disks and stellar halos has also been reported by other studies (e.g. Bakos et al. 2008; Bakos & Trujillo 2012; Yoachim et al. 2010, 2012; González Delgado et al. 2014). In a follow-up of our current work, we plan to explore their possible progenitors at moderate redshift.

#### ACKNOWLEDGEMENTS

We acknowledge the anonymous referee for a constructive report that significantly improved this paper. This project was supported by the NSF grants of China No.11573017 and 11733006. We acknowledge support of the CANDELS program HST-GO-12060 by NASA through a grant from the Space Telescope Science Institute, which is operated by the Association of Universities for Research in Astronomy, Incorporated, under NASA contract NAS5-26555. S.M.F., Y.G., D.C.K., and H.M.Y. acknowledge partial support from US NSF grant AST-16-15730. X.Z.Z. thanks support from the National Key Research and Development Program of China (No. 2017YFA0402703), NSFC (grant 11773076) and the Chinese Academy of Sciences (CAS) through a grant to the CAS South America Center for Astronomy (CASSACA) in Santiago, Chile.

#### REFERENCES

- Bakos, J., & Trujillo, I. 2012, ArXiv e-prints, arXiv:1204.3082
- Bakos, J., Trujillo, I., & Pohlen, M. 2008, ApJL, 683, L103
- Barro, G., Faber, S. M., Pérez-González, P. G., et al. 2013, ApJ, 765, 104
- Barro, G., Faber, S. M., Koo, D. C., et al. 2017, ApJ, 840, 47
- Baugh, C. M., Cole, S., & Frenk, C. S. 1996, MNRAS, 283, 1361



- Beckwith, S. V. W., Stiavelli, M., Koekemoer, A. M., et al. 2006, *AJ*, 132, 1729
- Bekki, K., & Chiba, M. 2001, *ApJ*, 558, 666
- Bell, E. F., Zucker, D. B., Belokurov, V., et al. 2008, *ApJ*, 680, 295
- Bender, R., Doebereiner, S., & Moellenhoff, C. 1988, *A&AS*, 74, 385
- Bender, R., Surma, P., Doebereiner, S., Moellenhoff, C., & Madejsky, R. 1989, *A&A*, 217, 35
- Bertin, E., & Arnouts, S. 1996, *A&AS*, 117, 393
- Bournaud, F., Dekel, A., Teyssier, R., et al. 2011, *ApJL*, 741, L33
- Brammer, G. B., van Dokkum, P. G., & Coppi, P. 2008, *ApJ*, 686, 1503
- Bruce, V. A., Dunlop, J. S., Cirasuolo, M., et al. 2012, *MNRAS*, 427, 1666
- Cacciato, M., Dekel, A., & Genel, S. 2012, *MNRAS*, 421, 818
- Carter, D. 1978, *MNRAS*, 182, 797
- Ceverino, D., Klypin, A., Klimek, E. S., et al. 2014, *MNRAS*, 442, 1545
- Chabrier, G. 2003, *PASP*, 115, 763
- Cheung, E., Athanassoula, E., Masters, K. L., et al. 2013, *ApJ*, 779, 162
- Cooper, A. P., D'Souza, R., Kauffmann, G., et al. 2013, *MNRAS*, 434, 3348
- Cooper, A. P., Cole, S., Frenk, C. S., et al. 2010, *MNRAS*, 406, 744
- Dahlen, T., Mobasher, B., Faber, S. M., et al. 2013, *ApJ*, 775, 93
- de Jong, R. S., Seth, A. C., Bell, E. F., et al. 2007, in *IAU Symposium*, Vol. 241, *Stellar Populations as Building Blocks of Galaxies*, ed. A. Vazdekis & R. Peletier, 503–504
- De Lucia, G. 2012, *Astronomische Nachrichten*, 333, 460
- De Lucia, G., & Helmi, A. 2008, *MNRAS*, 391, 14
- Dekel, A., Sari, R., & Ceverino, D. 2009, *ApJ*, 703, 785
- Eggen, O. J., Lynden-Bell, D., & Sandage, A. R. 1962, *ApJ*, 136, 748
- Elmegreen, B. G., Bournaud, F., & Elmegreen, D. M. 2008, *ApJ*, 688, 67
- Erwin, P., & Debattista, V. P. 2013, *MNRAS*, 431, 3060
- Erwin, P., & Sparke, L. S. 2002, *AJ*, 124, 65
- Fang, J. J., Faber, S. M., Koo, D. C., et al. 2017, *ArXiv e-prints*, arXiv:1710.05489
- Ferguson, A. M. N., Irwin, M. J., Ibata, R. A., Lewis, G. F., & Tanvir, N. R. 2002, *AJ*, 124, 1452
- Forbes, J., Krumholz, M., & Burkert, A. 2012, *ApJ*, 754, 48
- Forbes, J. C., Krumholz, M. R., Burkert, A., & Dekel, A. 2014, *MNRAS*, 438, 1552
- Galametz, A., Grazian, A., Fontana, A., et al. 2013, *ApJS*, 206, 10
- Genzel, R., Newman, S., Jones, T., et al. 2011, *ApJ*, 733, 101
- Gilbert, K. M., Guhathakurta, P., Kollipara, P., et al. 2009, *ApJ*, 705, 1275
- González Delgado, R. M., Pérez, E., Cid Fernandes, R., et al. 2014, *A&A*, 562, A47
- Grogin, N. A., Kocevski, D. D., Faber, S. M., et al. 2011, *ApJS*, 197, 35
- Guhathakurta, P., Gilbert, K. M., Kalirai, J. S., et al. 2005, in *Bulletin of the American Astronomical Society*, Vol. 37, *American Astronomical Society Meeting Abstracts*, 1386
- Guo, Y., Ferguson, H. C., Giavalisco, M., et al. 2013, *ApJS*, 207, 24
- Guo, Y., Ferguson, H. C., Bell, E. F., et al. 2015, *ApJ*, 800, 39
- Hao, C. N., Mao, S., Deng, Z. G., Xia, X. Y., & Wu, H. 2006, *MNRAS*, 370, 1339
- Hathi, N. P., Ferreras, I., Pasquali, A., et al. 2009, *ApJ*, 690, 1866
- Helmi, A. 2008, *A&A Rv*, 15, 145
- Huertas-Company, M., Pérez-González, P. G., Mei, S., et al. 2015, *ApJ*, 809, 95
- Ibata, R., Martin, N. F., Irwin, M., et al. 2007, *ApJ*, 671, 1591
- Ibata, R., Mouhcine, M., & Rejkuba, M. 2009, *MNRAS*, 395, 126
- Irwin, M. J., Ferguson, A. M. N., Ibata, R. A., Lewis, G. F., & Tanvir, N. R. 2005, *ApJL*, 628, L105
- Jedrzejewski, R. I. 1987, *MNRAS*, 226, 747
- Johnston, K. V., Bullock, J. S., Sharma, S., et al. 2008, *ApJ*, 689, 936
- Kauffmann, G., White, S. D. M., & Guiderdoni, B. 1993, *MNRAS*, 264, 201
- Koekemoer, A. M., Faber, S. M., Ferguson, H. C., et al. 2011, *ApJS*, 197, 36
- Kormendy, J. 1993, in *IAU Symposium*, Vol. 153, *Galactic Bulges*, ed. H. Dejonghe & H. J. Habing, 209
- Kormendy, J. 2013, *Secular Evolution in Disk Galaxies*, ed. J. Falcón-Barroso & J. H. Knapen, 1
- Kormendy, J., & Illingworth, G. 1982, *ApJ*, 256, 460
- Kormendy, J., & Kennicutt, Jr., R. C. 2004, *ARA&A*, 42, 603
- Krumholz, M., & Burkert, A. 2010, *ApJ*, 724, 895
- Laidler, V. G., Papovich, C., Grogin, N. A., et al. 2007, *PASP*, 119, 1325
- Lauer, T. R. 1985, *MNRAS*, 216, 429
- Liu, F. S., Jiang, D., Guo, Y., et al. 2016, *ApJL*, 822, L25

- Margalef-Bentabol, B., Conselice, C. J., Mortlock, A., et al. 2016, *MNRAS*, 461, 2728
- Martínez-Delgado, D., Gabany, R. J., Crawford, K., et al. 2010, *AJ*, 140, 962
- McConnachie, A. W., Irwin, M. J., Ibata, R. A., et al. 2009, *Nature*, 461, 66
- Mobasher, B., Dahlen, T., Ferguson, H. C., et al. 2015, *ApJ*, 808, 101
- Moster, B. P., Naab, T., & White, S. D. M. 2013, *MNRAS*, 428, 3121
- Mouhcine, M., Ferguson, H. C., Rich, R. M., Brown, T. M., & Smith, T. E. 2005a, *ApJ*, 633, 821
- Mouhcine, M., Ibata, R., & Rejkuba, M. 2010, *ApJL*, 714, L12
- Mouhcine, M., Rich, R. M., Ferguson, H. C., Brown, T. M., & Smith, T. E. 2005b, *ApJ*, 633, 828
- Noguchi, M. 1999, *ApJ*, 514, 77
- Papovich, C., Labbé, I., Quadri, R., et al. 2015, *ApJ*, 803, 26
- Peng, C. Y., Ho, L. C., Impey, C. D., & Rix, H.-W. 2002, *AJ*, 124, 266
- Pillepich, A., Vogelsberger, M., Deason, A., et al. 2014, *MNRAS*, 444, 237
- Purcell, C. W., Bullock, J. S., & Zentner, A. R. 2007, *ApJ*, 666, 20
- Samland, M., & Gerhard, O. E. 2003, *A&A*, 399, 961
- Sandage, A. 1986, *ARA&A*, 24, 421
- Santini, P., Ferguson, H. C., Fontana, A., et al. 2015, *ApJ*, 801, 97
- Searle, L., & Zinn, R. 1978, *ApJ*, 225, 357
- Starkeburg, E., Helmi, A., Morrison, H. L., et al. 2009, *ApJ*, 698, 567
- Steinmetz, M., & Muller, E. 1995, *MNRAS*, 276, 549
- Tonini, C., Mutch, S. J., Croton, D. J., & Wyithe, J. S. B. 2016a, *MNRAS*, 459, 4109
- Tonini, C., Mutch, S. J., Wyithe, J. S. B., & Croton, D. J. 2016b, *ArXiv e-prints*, arXiv:1606.06040
- Trujillo, I., & Bakos, J. 2013, *MNRAS*, 431, 1121
- van der Wel, A., Rix, H.-W., Wuyts, S., et al. 2011, *ApJ*, 730, 38
- van der Wel, A., Bell, E. F., Häussler, B., et al. 2012, *ApJS*, 203, 24
- van der Wel, A., Franx, M., van Dokkum, P. G., et al. 2014a, *ApJ*, 788, 28
- van der Wel, A., Chang, Y.-Y., Bell, E. F., et al. 2014b, *ApJL*, 792, L6
- Williams, R. J., Quadri, R. F., Franx, M., van Dokkum, P., & Labbé, I. 2009, *ApJ*, 691, 1879
- Wisnioski, E., Förster Schreiber, N. M., Wuyts, S., et al. 2015, *ApJ*, 799, 209
- Wuyts, S., Förster Schreiber, N. M., van der Wel, A., et al. 2011, *ApJ*, 742, 96
- Yoachim, P., Roškar, R., & Debattista, V. P. 2010, *ApJL*, 716, L4
- . 2012, *ApJ*, 752, 97
- Zheng, Z., Thilker, D. A., Heckman, T. M., et al. 2015, *ApJ*, 800, 120
- Zibetti, S., & Ferguson, A. M. N. 2004, *MNRAS*, 352, L6

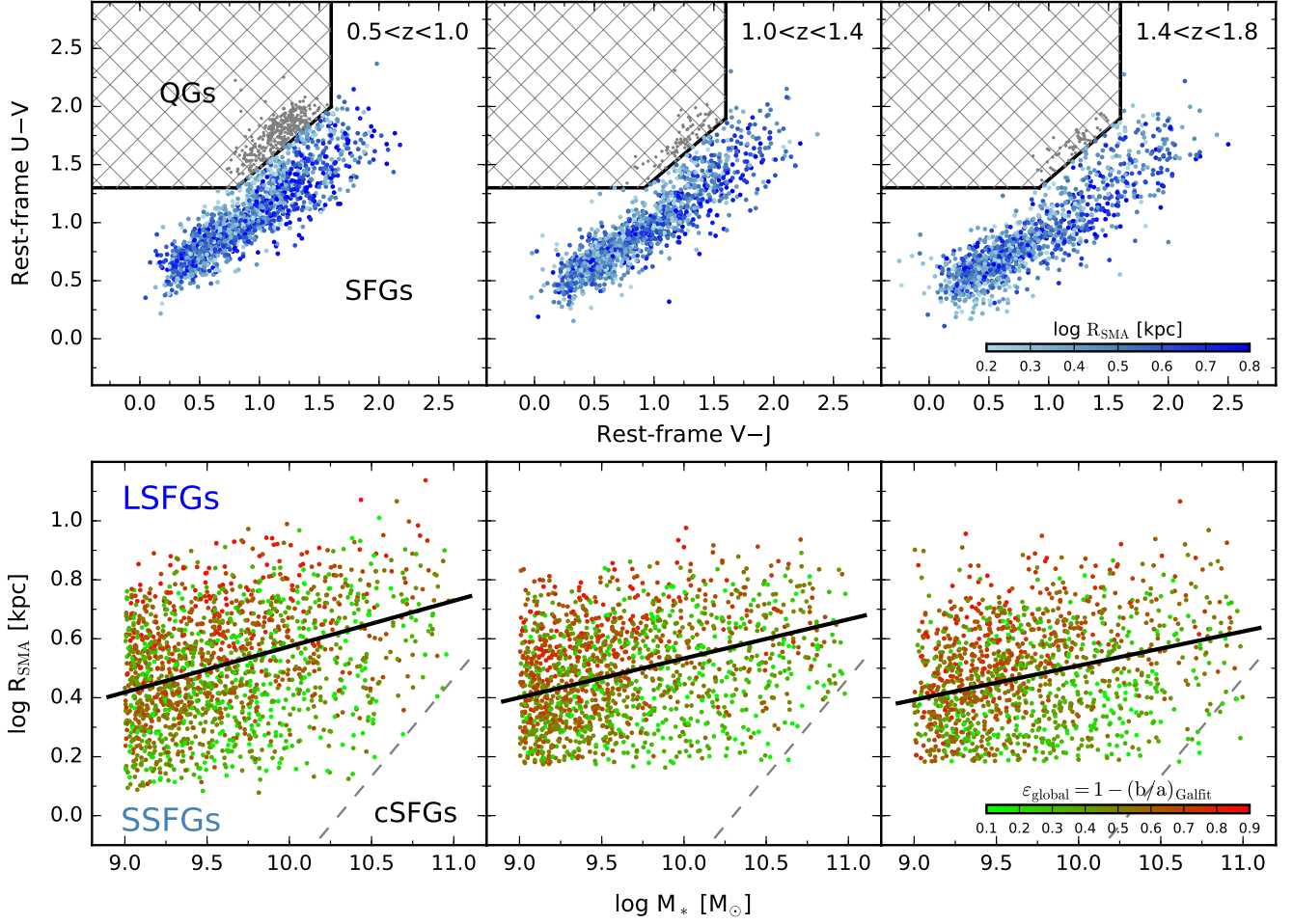


**Figure 1.** Rest-frame UVJ color-color diagrams (top) for our sample galaxies after applying the selection cuts and the size-mass relations (bottom) for UVJ-defined SFGs only in three redshift bins, respectively. In the top panels, the solid lines are the classification criteria of Williams et al. (2009). SFGs are shown with solid points and color coded by  $\log R_{\text{SMA}}$ . Quiescent galaxies are indicated by gray hatching. In the bottom panels, the solid black lines indicate the best-fit linear relations in three redshift bins, respectively. The vertical offsets from the relations ( $\Delta \log R_{\text{SMA}}$ ) are used to divide our SFGs into LSFGs ( $\Delta \log R_{\text{SMA}} > 0$ ) and SSFGs ( $\Delta \log R_{\text{SMA}} < 0$ ) in each redshift bin. The grey dashed lines indicate the classification criterion of compact and non-compact SFGs by Barro et al. (2013). Data points are color-coded by global ellipticity ( $\varepsilon_{\text{global}} = 1 - (b/a)_{\text{Galfit}}$ ).

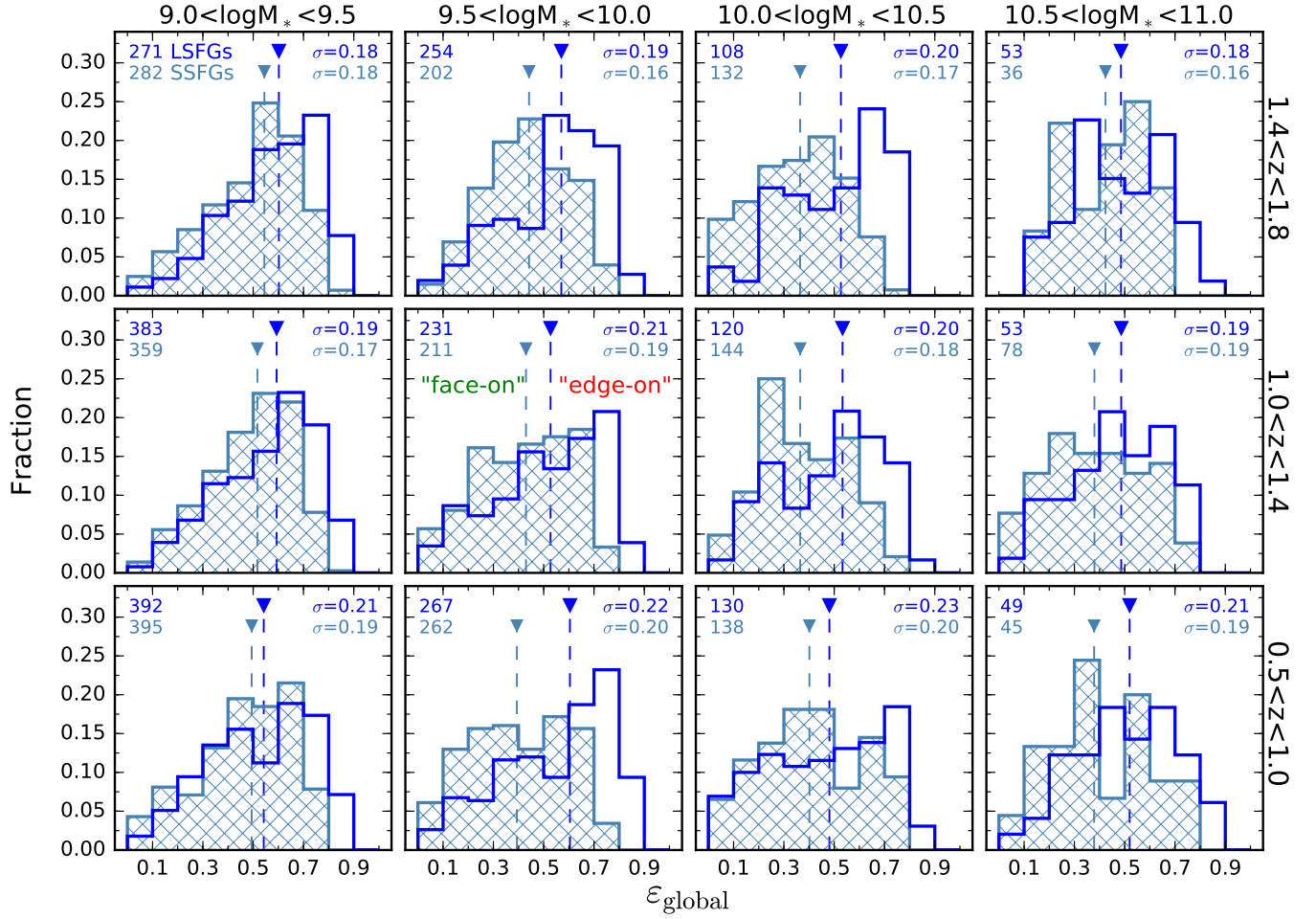


**Figure 2.** Distributions of global ellipticity for LSFs (blue) and SSFGs (steel blue) in each mass-redshift bin, respectively. The median values are indicated with triangles plus dashed lines. The standard deviations ( $\sigma$ ) are presented in the right-top corner of each panel. The galaxy numbers are presented in the left-top corner of each panel.



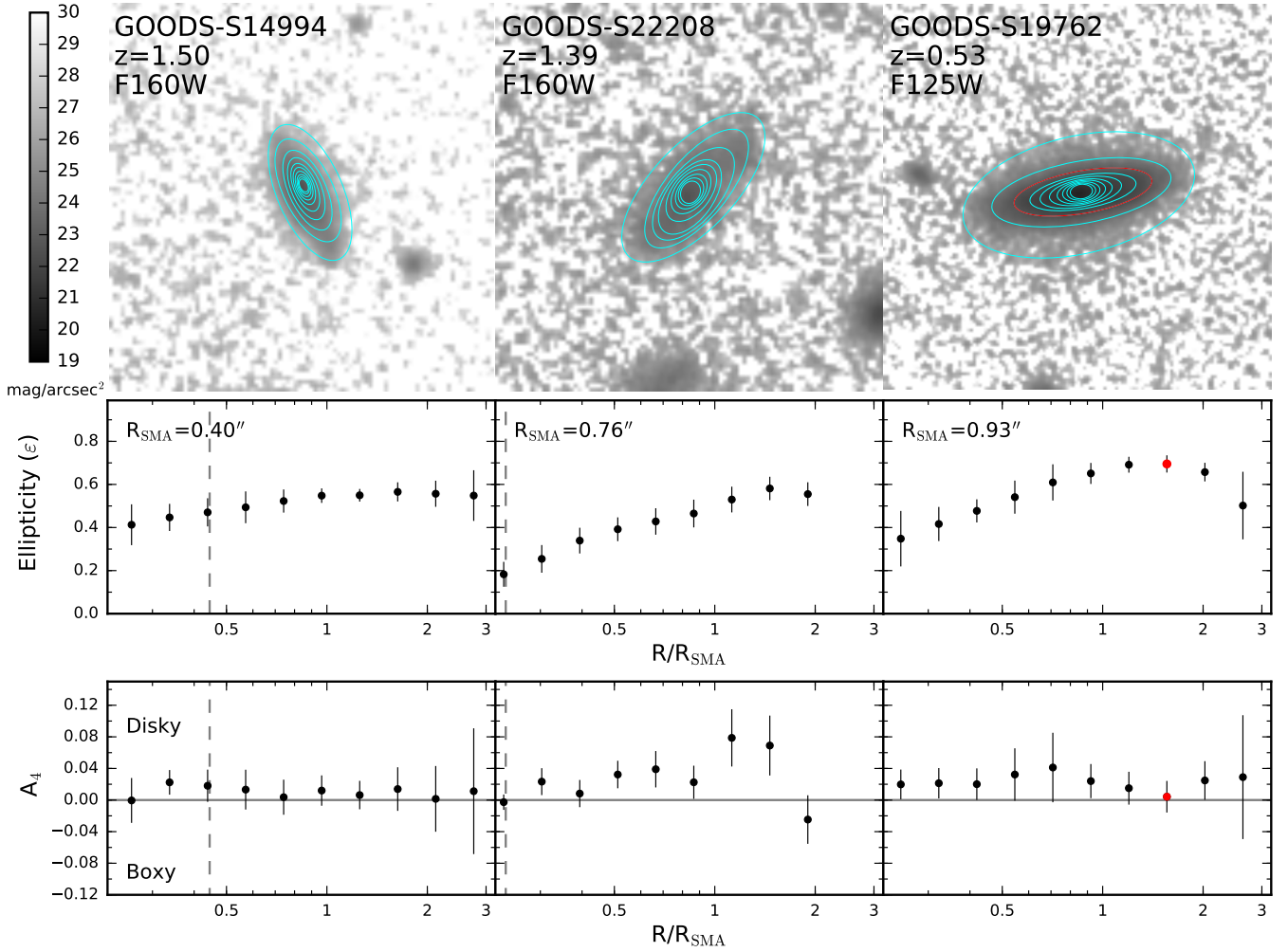


**Figure 3.** Example nearly edge-on galaxies GOODS-S 14994, GOODS-S 22208 and GOODS-S 19762 illustrating the measurement of isophotal shape profiles. In the top panels, the cyan ellipses are from our isophotal measurements by `IRAF/ellipse`. The red ellipse in the right panel indicates the position of the maximum ellipticity. The corresponding radial ellipticity profiles with errorbars are shown in the middle panels. The corresponding  $A_4$  profiles with errorbars are shown in the bottom panels. The vertical dashed lines in the middle and bottom panels indicate the FWHM of PSF (0.18''). The solid horizontal lines in the bottom panels indicate  $A_4 = 0$ .

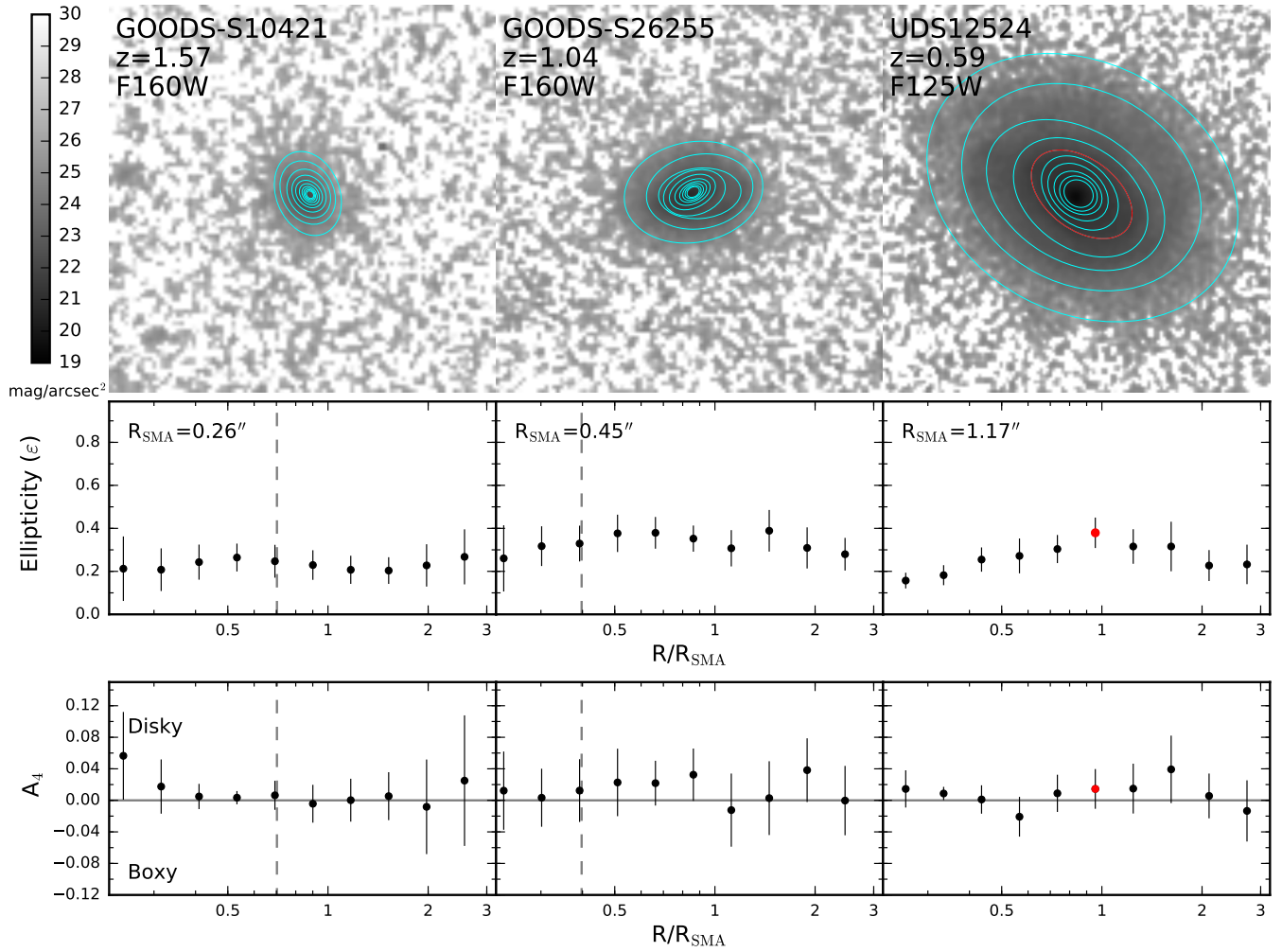


**Figure 4.** Example nearly face-on galaxies GOODS-S 10421, GOODS-S 26255 and UDS 12524 illustrating the measurement of isophotal shape profiles. The data points, error-bars and lines have the same meanings as those in Figure 3.

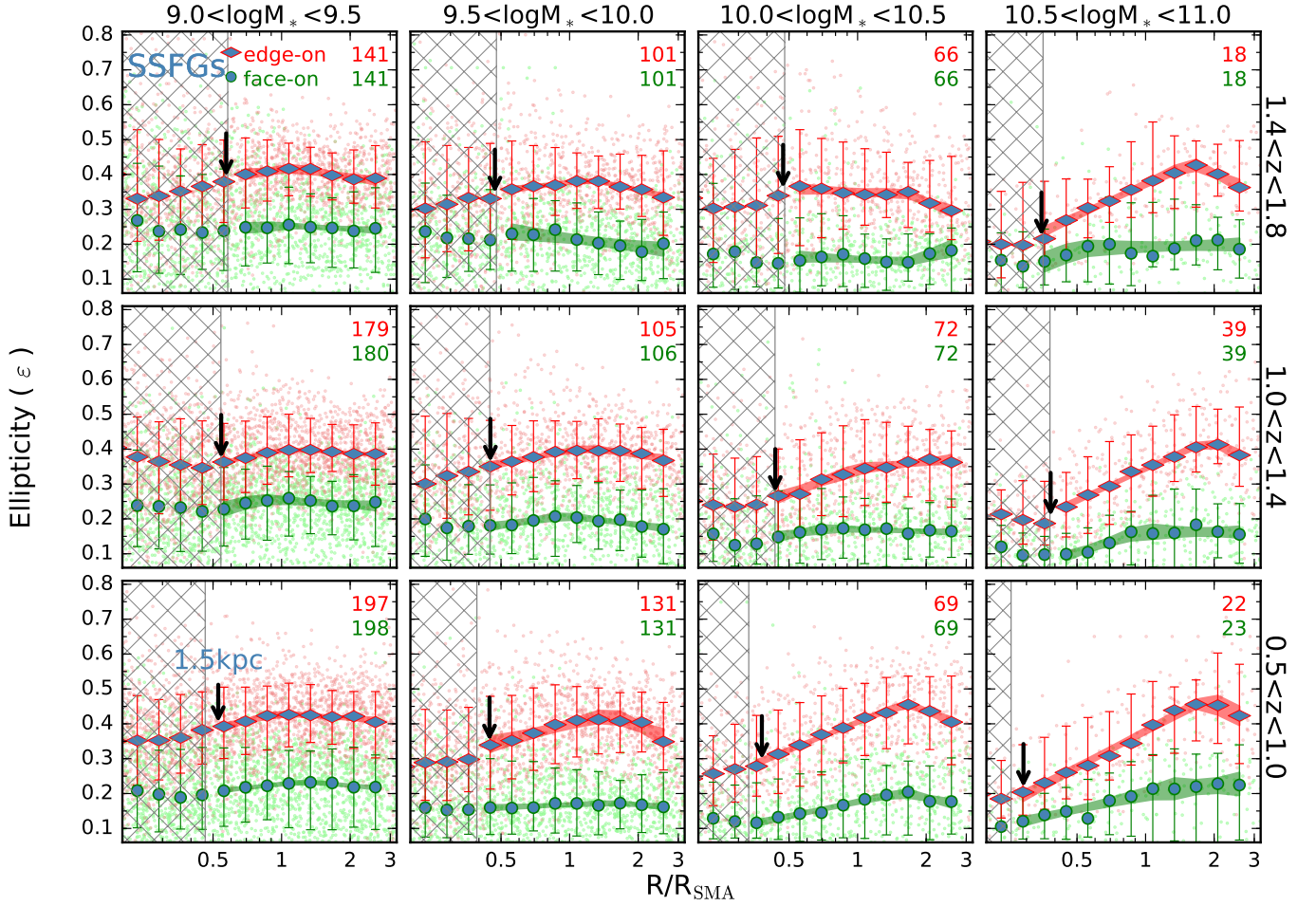


**Figure 5.** The composite ellipticity profiles as a function of normalised radius for the SSFGs in classified mass-redshift bins. The steel blue diamonds with red edge represent the median values of ellipticities at every given radius for edge-on systems, followed by 68% confidence intervals. The steel blue circles with green edge represent the median values of ellipticities at every given radius for face-on systems, followed by 68% confidence intervals. The shade regions indicate the ranges affected significantly by PSF smoothing ( $0.18''$ ). The galaxy number of each class is shown on the right-top corner of each panel. The thick black arrows indicate the position of  $R_{\text{SMA}} = 1.5\text{kpc}$  in each bin. The observed data are shown with tiny dots for edge-on (red) and face-on (green) systems, respectively. The shade regions show the best segmented models with  $2\sigma$  lower and upper limits for edge-on (red) and face-on (green) systems, respectively.

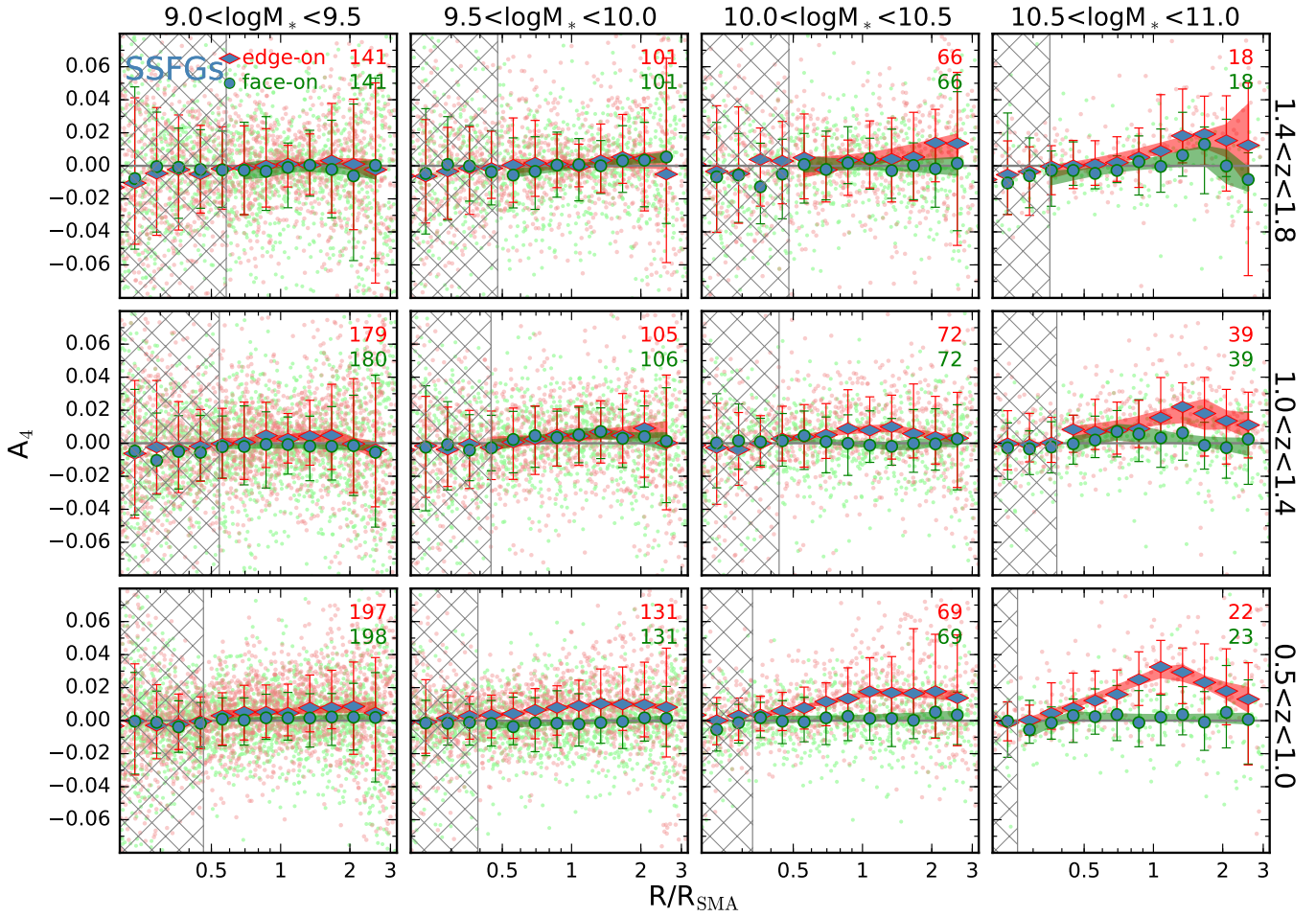


**Figure 6.** The composite  $A_4$  as a function of normalised radius for the SSFGs. The data points, error-bars and lines have the same meanings as those in Figure 5.  $A_4 > 0$  indicates disk, whereas  $A_4 < 0$  indicates boxy.



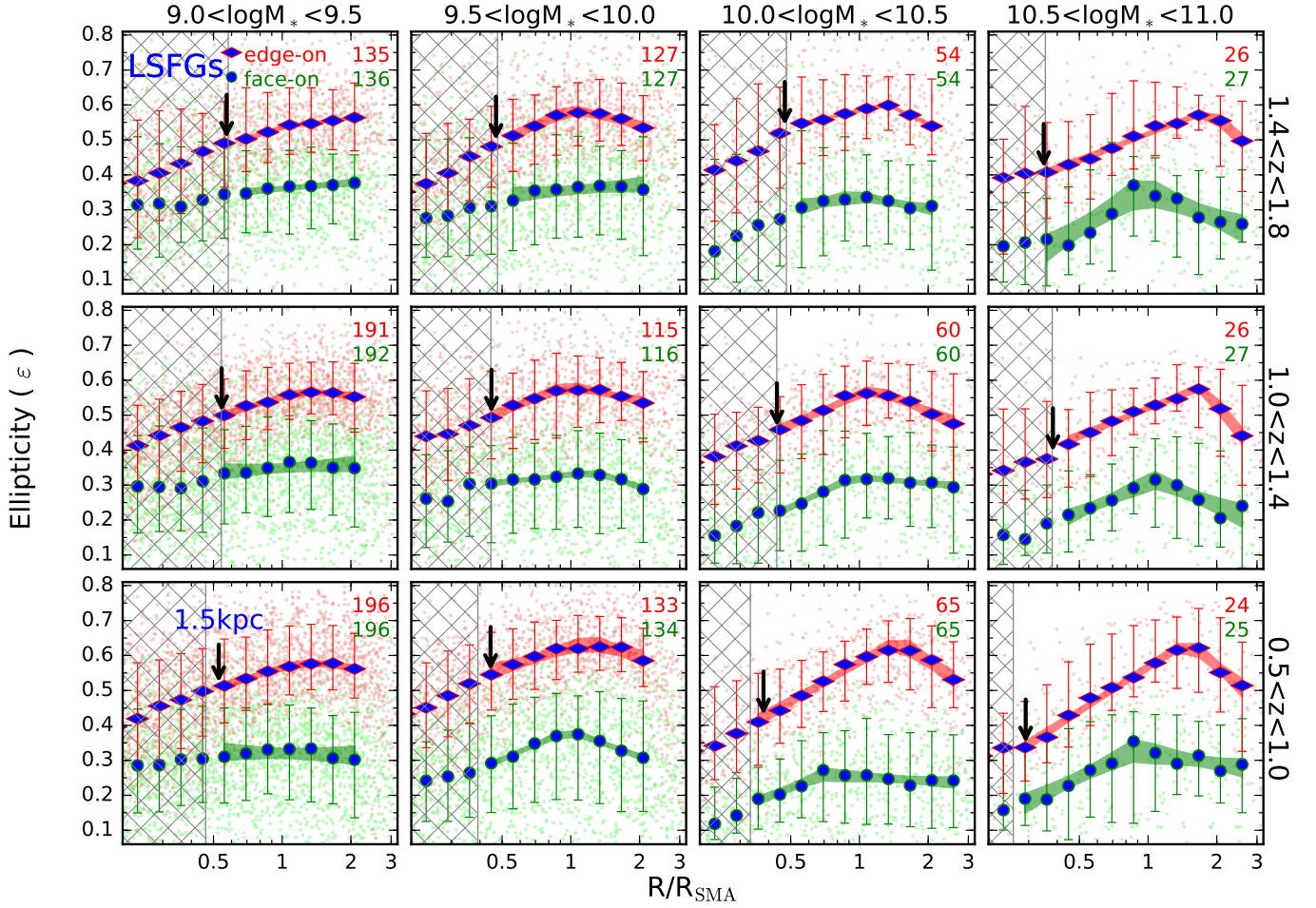


**Figure 7.** The composite ellipticity profiles as a function of normalised radius for the LSFs in classified mass-redshift bins. The blue diamonds with red edge represent the median values of ellipticities at every given radius for edge-on systems, followed by 68% confidence intervals. The blue circles with green edge represent the median values of ellipticities at every given radius for face-on systems, followed by 68% confidence intervals. The shade regions indicate the ranges affected significantly by PSF smoothing ( $0.18''$ ). The galaxy number of each class is shown on the right-top corner of each panel. The thick black arrows indicate the position of  $R_{\text{SMA}} = 1.5 \text{ kpc}$  in each bin. The observed data are shown with tiny dots for edge-on (red) and face-on (green) systems, respectively. The shade regions show the best segmented models with  $2\sigma$  lower and upper limits for edge-on (red) and face-on (green) systems, respectively.

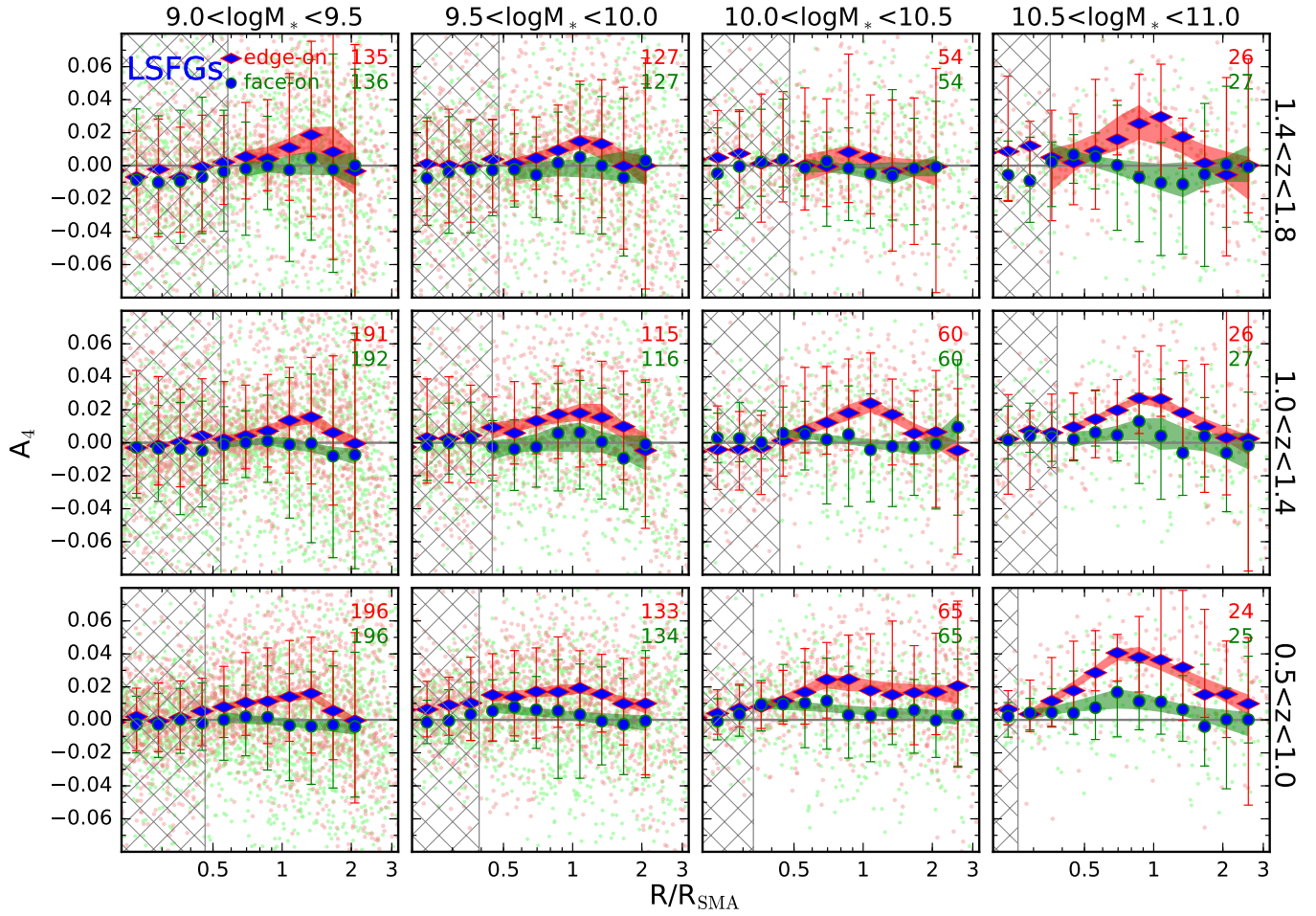


**Figure 8.** The composite  $A_4$  as a function of normalised radius for the LSFs. The data points, error-bars and lines have the same meanings as those in Figure 7.  $A_4 > 0$  indicates disk, whereas  $A_4 < 0$  indicates boxy.

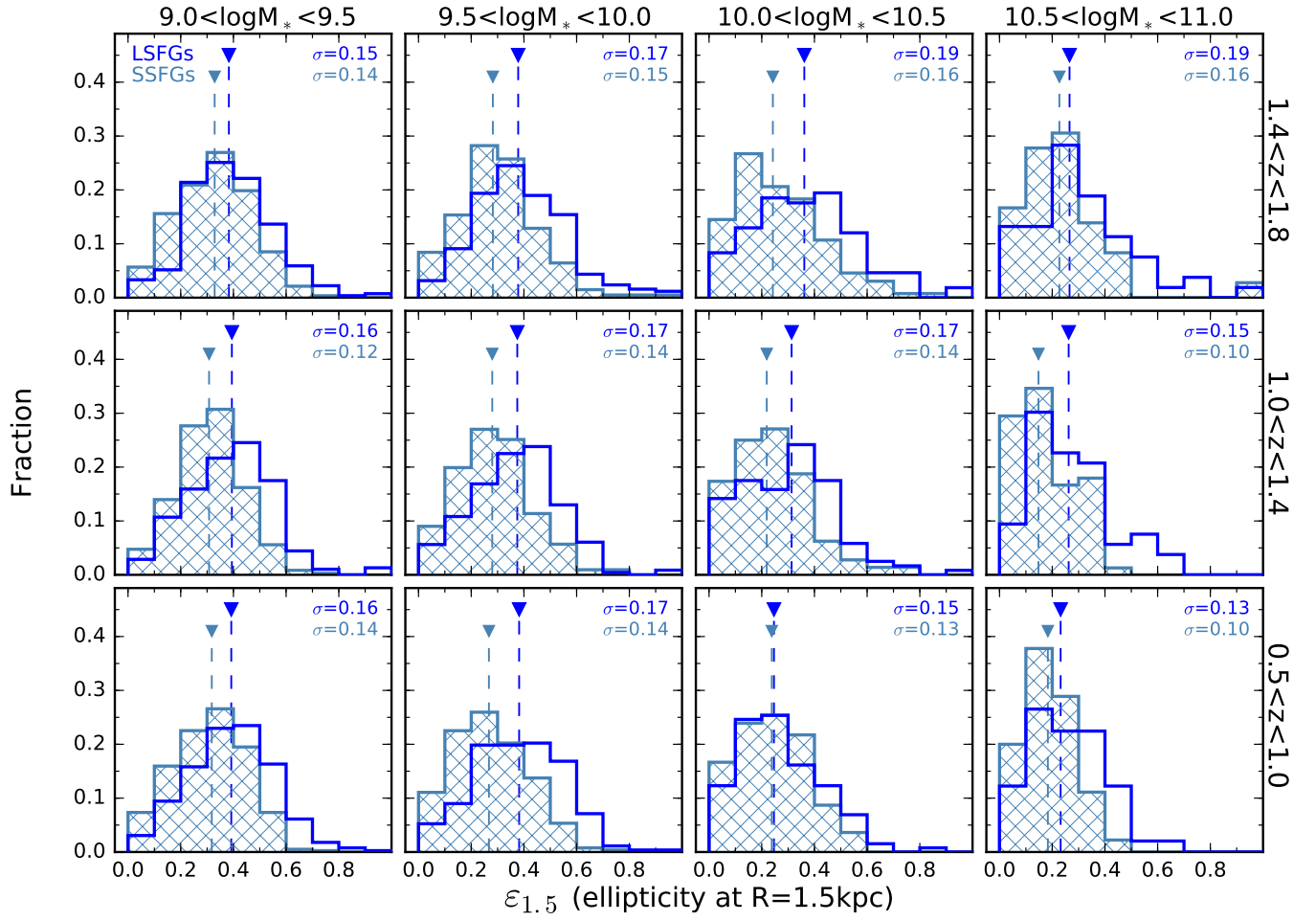


**Figure 9.** Distributions of ellipticity at the position of  $R_{SMA} = 1.5 \text{ kpc}$  ( $\epsilon_{1.5}$ ) for LSFs (blue) and SSFGs (steel blue) in each mass-redshift bin. The median values are indicated with triangles plus dashed lines. The standard deviations ( $\sigma$ ) are presented in the right-top corner of each panel.



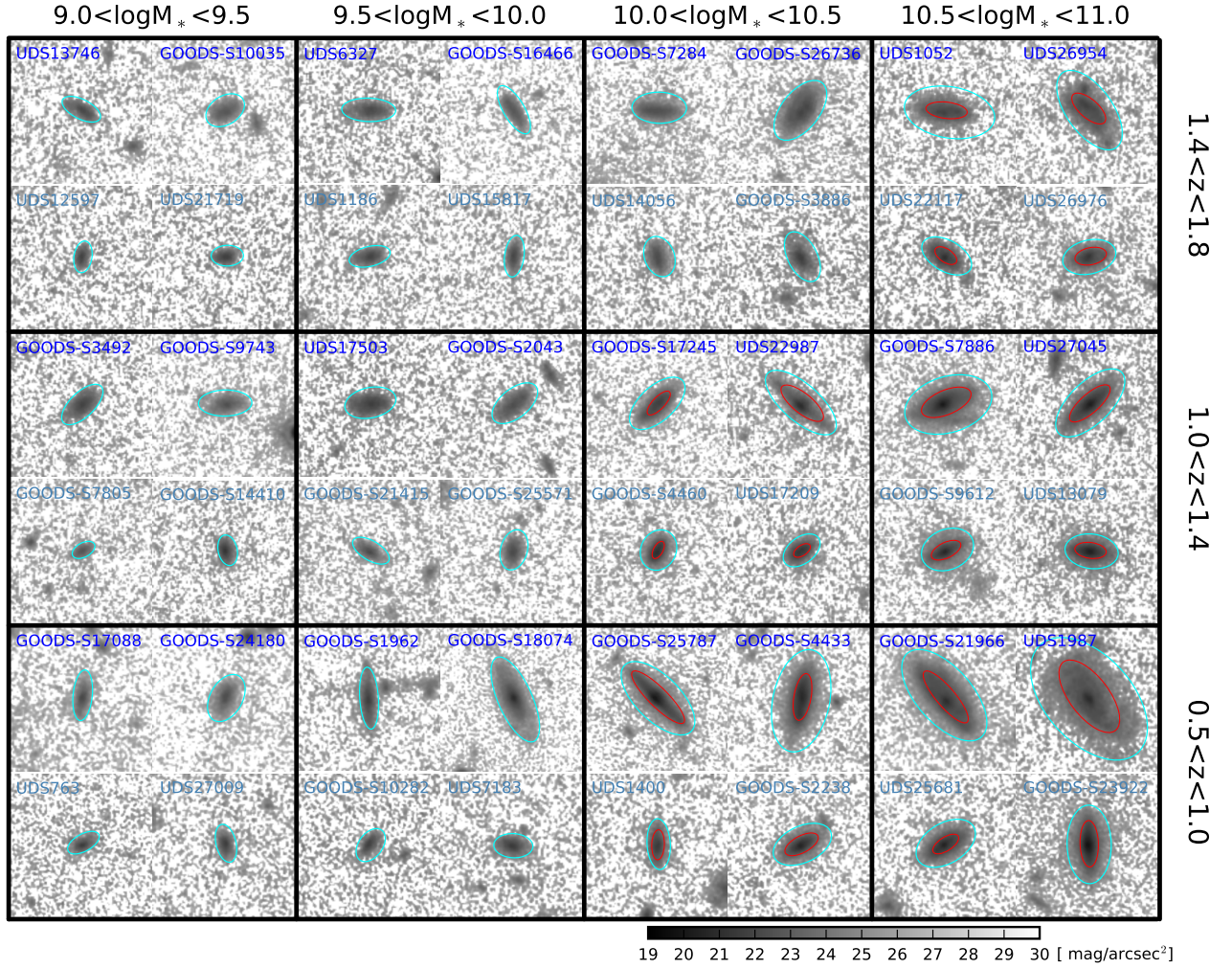


**Figure 10.** Cut-out images of example edge-on galaxies in F160W (for  $1.0 < z < 1.8$ ) and F125W (for  $0.5 < z < 1.0$ ) in every mass-redshift bin. The size of each cut-out image is  $50 \times 50$  kpc. The cyan ellipse in each cut-out image indicates the outermost isophote we measured, which is close to the position of  $\sim 3R_{\text{SMA}}$ . The red ellipses indicate the positions of maximum ellipticity in the  $\epsilon$  profiles of some galaxies with diffuse halo-like stellar components. In each bin, the upper images are for LSFs, whereas the lower ones are for SSFGs.



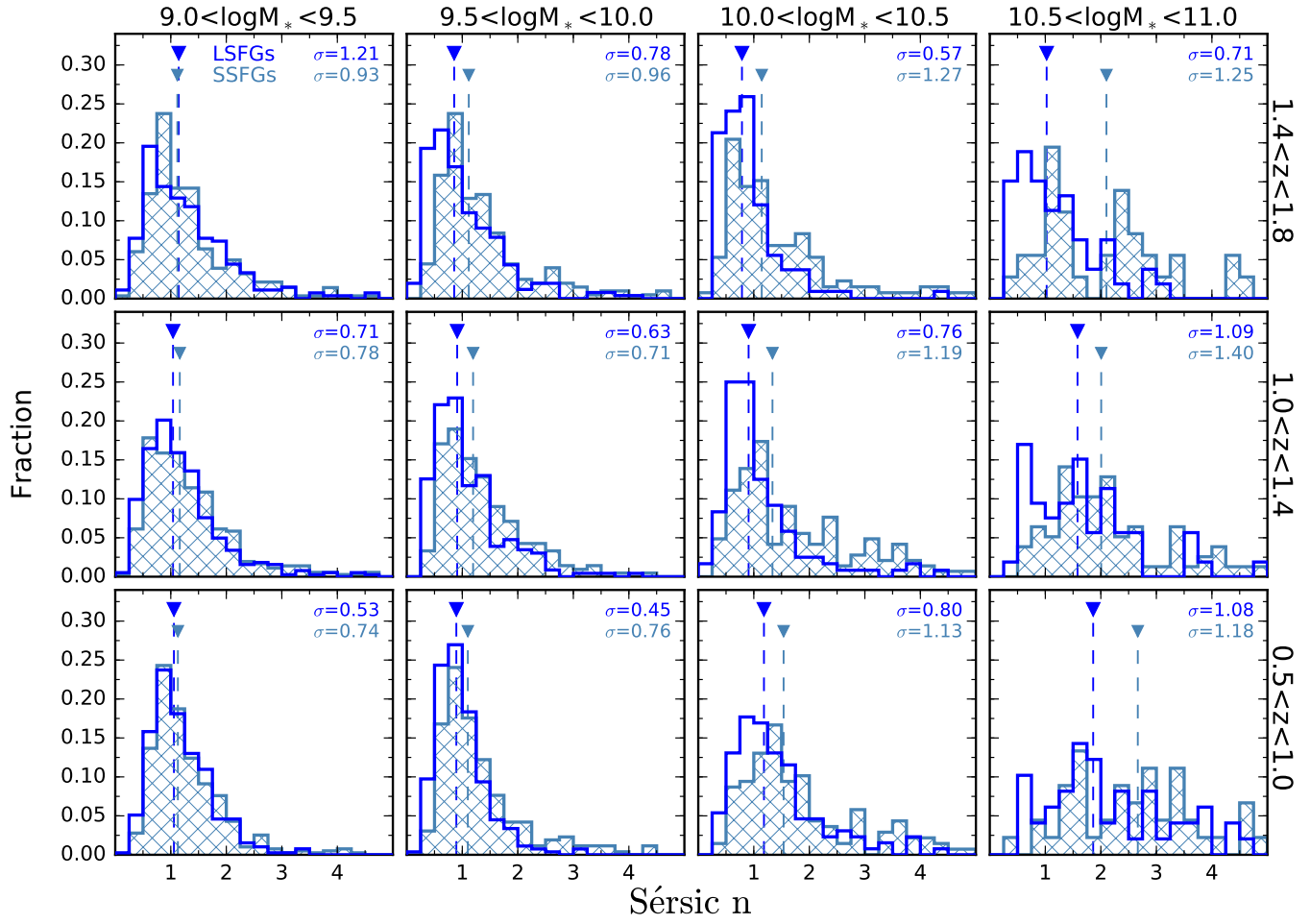


**Figure 11.** Distributions of Sérsic Index  $n$  for the LSFGs (blue) and SSFGs (steel blue) in every mass-redshift bin, respectively. The median values are indicated with triangles plus dashed lines. The standard deviations ( $\sigma$ ) are presented in the right-top corner of each panel.

**Table 1.** Sample Selection Cuts

Cut	GOODS-S	UDS	Combined
Full catalog	34,930 (100.0%)	35,932 (100.0%)	70,862 (100.0%)
F160W( $H$ ) < 24.5	8,293 (23.7%)	9,671 (26.9%)	17,964 (25.4%)
SE PhotFlag = 0	8,104 (23.2%)	9,151 (25.5%)	17,255 (24.4%)
SE CLASS_STAR < 0.9	7,891 (22.6%)	8,933 (24.9%)	16,824 (23.7%)
$0.5 < z < 1.8$	4,753 (13.6%)	5,735 (16.0%)	10,488 (14.8%)
$9.0 < \log M^* < 11.0$	3,261 (9.3%)	3,964 (11.0%)	7,225 (10.2%)
GALFIT flag = 0	2,868 (8.2%)	3,555 (9.9%)	6,423 (9.1%)
ISO PhotFlag = 0	2,690 (7.7%)	3,434 (9.6%)	6,124 (8.6%)
R <sub>SMA</sub> > 0.18''	2,250 (6.4%)	2,829 (7.9%)	5,079 (7.2%)
UVJ-defined SFGs	2,036 (5.8%)	2,571 (7.2%)	4,607 (6.5%)
non-compact SFGs	2,033 (5.8%)	2,562 (7.1%)	4,595 (6.5%)

**Table 2.** Parameters of the best linear fits to the size-mass relations

Redshift Range	Slope $a$	Zeropoint $b$
$0.5 < z < 1.0$	0.155	-0.978
$1.0 < z < 1.4$	0.133	-0.793
$1.4 < z < 1.8$	0.116	-0.651

Table 3. Best-fit parameters for the ellipticity and  $A_4$  profiles

Stellar Mass	Sub-class	1.4 < z < 1.8					1.0 < z < 1.4					0.5 < z < 1.0				
		Slope	Intercept	R-squared	Break $\bar{R}^*$	Break $\bar{R}^*$	Slope	Intercept	R-squared	Break $\bar{R}^*$	Break $\bar{R}^*$	Slope	Intercept	R-squared	Break $\bar{R}^*$	
Best-fit parameters of ellipticity profiles for SSFGs (Figure 5)																
9.0 < logM <sub>*</sub> < 9.5	face-on	0.033±0.098	0.252±0.011	0.59	1.06	0.184±0.133	0.275±0.027	0.60	0.80	0.070±0.014	0.227±0.002	0.92	1.26			
	edge-on	-0.033±0.016	0.254±0.017	...	...	-0.039±0.023	0.253±0.031	...	...	-0.057±0.014	0.240±0.002	...	...			
	face-on	0.085±0.052	0.414±0.005	0.87	1.12	0.141±0.017	0.398±0.003	0.98	1.03	0.160±0.036	0.433±0.006	0.91	0.96			
9.5 < logM <sub>*</sub> < 10.0	face-on	-0.101±0.031	0.424±0.007	...	...	-0.037±0.007	0.400±0.003	...	...	-0.045±0.015	0.429±0.005	...	...			
	edge-on	-0.075±0.021	0.216±0.005	0.69	...	0.095±0.029	0.211±0.007	0.86	0.96	0.025±0.012	0.168±0.002	0.64	1.60			
	face-on	0.080±0.018	0.377±0.002	0.96	1.25	0.121±0.019	0.395±0.003	0.92	1.18	0.164±0.035	0.399±0.006	0.87	1.51			
10.0 < logM <sub>*</sub> < 10.5	face-on	-0.149±0.017	0.400±0.002	...	...	-0.091±0.025	0.411±0.003	...	...	-0.287±0.089	0.480±0.004	...	...			
	edge-on	0.196±0.147	0.107±0.003	0.71	1.67	0.110±0.053	0.188±0.014	0.62	0.73	0.137±0.012	0.176±0.003	0.97	1.57			
	face-on	-0.029±0.022	0.157±0.003	...	...	-0.019±0.013	0.170±0.012	...	...	-0.147±0.050	0.232±0.002	...	...			
10.5 < logM <sub>*</sub> < 11.0	edge-on	-0.032±0.028	0.351±0.004	0.92	1.66	0.234±0.043	0.344±0.010	0.97	1.01	0.265±0.012	0.405±0.003	0.99	1.61			
	face-on	0.250±0.201	0.260±0.080	0.64	0.51	0.063±0.029	0.344±0.009	...	...	-0.255±0.045	0.513±0.001	...	...			
	edge-on	0.016±0.024	0.192±0.043	...	...	-0.003±0.040	0.163±0.015	...	...	0.048±0.088	0.208±0.009	...	...			
9.0 < logM <sub>*</sub> < 9.5	face-on	0.015±0.035	-0.001±0.004	0.53	1.05	-0.001±0.002	-0.002±0.000	0.53	...	0.003±0.001	0.001±0.000	0.68	1.78			
	edge-on	-0.005±0.009	-0.000±0.003	...	...	...	...	...	...	-0.002±0.013	0.003±0.000	...	...			
	face-on	0.008±0.004	0.000±0.000	0.65	1.86	0.011±0.005	0.003±0.001	0.78	1.59	0.007±0.002	0.006±0.000	0.55	...			
9.5 < logM <sub>*</sub> < 10.0	face-on	-0.034±0.034	0.012±0.000	...	...	-0.045±0.017	0.014±0.001	...	...	...	...	...	...			
	edge-on	0.014±0.003	-0.001±0.000	0.84	...	0.018±0.006	0.005±0.001	0.74	1.19	0.005±0.001	-0.001±0.000	0.67	...			
	face-on	0.006±0.005	0.001±0.001	0.52	...	-0.017±0.011	0.008±0.002	...	...	...	...	...	...			
10.0 < logM <sub>*</sub> < 10.5	face-on	-0.002±0.005	0.001±0.001	0.52	...	0.011±0.004	0.004±0.001	0.56	...	0.015±0.001	0.009±0.000	0.99	1.44			
	edge-on	0.020±0.007	0.004±0.001	0.59	...	-0.009±0.003	-0.001±0.001	0.66	1.37	-0.010±0.005	0.012±0.000	...	...			
	face-on	0.021±0.006	0.002±0.001	0.69	...	0.013±0.014	-0.004±0.000	...	...	0.003±0.002	0.002±0.001	0.58	...			
10.5 < logM <sub>*</sub> < 11.0	face-on	-0.082±0.064	0.025±0.001	...	...	-0.025±0.006	0.012±0.000	...	...	0.028±0.002	0.016±0.001	0.98	1.19			
	edge-on	0.029±0.005	0.009±0.001	0.86	1.80	0.041±0.019	0.013±0.005	0.63	0.70	-0.008±0.007	0.018±0.001	...	...			
	face-on	-0.028±0.140	0.024±0.002	...	...	-0.016±0.009	0.005±0.007	...	...	0.049±0.024	0.021±0.011	0.72	0.43			
edge-on	0.029±0.005	0.009±0.001	0.86	1.80	0.026±0.008	0.015±0.002	0.71	1.49	-0.002±0.003	0.002±0.007	...	...				
face-on	-0.028±0.140	0.024±0.002	...	...	-0.035±0.032	0.025±0.001	...	...	0.052±0.004	0.028±0.001	0.98	1.19				
edge-on	0.029±0.005	0.009±0.001	0.86	1.80	0.026±0.008	0.015±0.002	0.71	1.49	-0.002±0.003	0.002±0.007	...	...				
face-on	-0.028±0.140	0.024±0.002	...	...	-0.035±0.032	0.025±0.001	...	...	0.052±0.004	0.028±0.001	0.98	1.19				
edge-on	0.029±0.005	0.009±0.001	0.86	1.80	0.026±0.008	0.015±0.002	0.71	1.49	-0.002±0.003	0.002±0.007	...	...				
face-on	-0.028±0.140	0.024±0.002	...	...	-0.035±0.032	0.025±0.001	...	...	0.052±0.004	0.028±0.001	0.98	1.19				
edge-on	0.029±0.005	0.009±0.001	0.86	1.80	0.026±0.008	0.015±0.002	0.71	1.49	-0.002±0.003	0.002±0.007	...	...				

Best-fit parameters for the  $A_4$  profiles of SSFGs (Figure 6)

Table 3. (continued)

Stellar Mass	Sub-class	1.4 < z < 1.8				1.0 < z < 1.4				0.5 < z < 1.0			
		Slope	Intercept	R-squared	Break $\tilde{R}^*$	Slope	Intercept	R-squared	Break $\tilde{R}^*$	Slope	Intercept	R-squared	Break $\tilde{R}^*$
Best-fit parameters of ellipticity profiles for LSFs (Figure 7)													
9.0 < logM <sub>*</sub> < 9.5	face-on	0.055±0.010	0.361±0.002	0.87	...	0.037±0.023	0.349±0.004	0.54	...	-0.017±0.028	0.320±0.005	0.07	...
		...	...	...	...	...	...	...	...	...	...	...	...
	edge-on	0.201±0.033	0.535±0.004	1.00	1.07	0.195±0.023	0.552±0.003	0.98	1.23	0.195±0.025	0.564±0.004	0.98	1.23
		0.075±0.008	0.539±0.003	...	...	-0.065±0.035	0.575±0.004	...	...	-0.078±0.034	0.589±0.002	...	...
9.5 < logM <sub>*</sub> < 10.0	face-on	0.053±0.023	0.356±0.004	0.51	...	0.069±0.014	0.330±0.003	0.95	1.27	0.283±0.021	0.388±0.005	0.99	0.98
		...	...	...	...	-0.211±0.032	0.358±0.004	...	...	-0.241±0.023	0.383±0.006	...	...
	edge-on	0.307±0.059	0.589±0.011	0.96	1.00	0.263±0.040	0.589±0.009	0.95	0.96	0.200±0.043	0.624±0.008	0.89	1.21
		-0.153±0.033	0.589±0.013	...	...	-0.136±0.033	0.582±0.011	...	...	-0.201±0.082	0.656±0.010	...	...
10.0 < logM <sub>*</sub> < 10.5	face-on	0.122±0.080	0.341±0.013	0.79	0.97	0.310±0.026	0.331±0.006	0.99	0.95	0.261±0.042	0.300±0.015	0.92	0.69
		-0.116±0.039	0.338±0.010	...	...	-0.057±0.017	0.322±0.006	...	...	-0.039±0.026	0.253±0.020	...	...
	edge-on	0.152±0.010	0.584±0.001	1.00	1.31	0.284±0.026	0.559±0.005	0.97	1.15	0.372±0.023	0.581±0.005	0.98	1.47
		-0.310±0.015	0.639±0.002	...	...	-0.279±0.044	0.594±0.006	...	...	-0.446±0.088	0.718±0.004	...	...
10.5 < logM <sub>*</sub> < 11.0	face-on	0.396±0.082	0.367±0.025	0.87	0.95	0.277±0.061	0.306±0.014	0.90	1.07	0.316±0.052	0.347±0.019	0.90	0.86
		-0.255±0.079	0.352±0.031	...	...	-0.266±0.061	0.322±0.017	...	...	-0.103±0.058	0.321±0.027	...	...
	edge-on	0.250±0.010	0.517±0.002	0.99	1.85	0.262±0.016	0.520±0.003	0.98	1.73	0.422±0.016	0.567±0.005	0.99	1.50
		-0.598±0.127	0.744±0.001	...	...	-0.812±0.154	0.776±0.003	...	...	-0.562±0.088	0.739±0.005	...	...
Best-fit parameters for the A <sub>4</sub> profiles of LSFs (Figure 8)													
9.0 < logM <sub>*</sub> < 9.5	face-on	0.012±0.021	0.000±0.002	0.59	1.32	0.011±0.007	0.002±0.001	0.86	0.93	-0.010±0.004	-0.001±0.001	0.61	...
		-0.018±0.033	0.004±0.001	...	...	-0.028±0.010	0.001±0.002	...	...	...	...	...	...
	edge-on	0.042±0.018	0.010±0.002	0.80	1.42	0.040±0.006	0.011±0.001	0.96	1.31	0.021±0.004	0.013±0.001	0.97	1.32
		-0.119±0.108	0.035±0.001	...	...	-0.086±0.016	0.026±0.001	...	...	-0.089±0.011	0.027±0.000	...	...
9.5 < logM <sub>*</sub> < 10.0	face-on	0.005±0.009	-0.002±0.002	0.55	...	0.023±0.018	0.004±0.005	0.54	1.01	-0.014±0.003	0.002±0.001	0.75	...
		...	...	...	...	-0.033±0.026	0.004±0.004	...	...	...	...	...	...
	edge-on	0.049±0.010	0.013±0.002	0.90	1.13	0.029±0.010	0.018±0.002	0.86	1.24	0.013±0.008	0.019±0.002	0.87	1.07
		-0.071±0.029	0.019±0.001	...	...	-0.102±0.029	0.030±0.003	...	...	-0.039±0.008	0.020±0.003	...	...
10.0 < logM <sub>*</sub> < 10.5	face-on	-0.013±0.011	-0.003±0.002	0.59	...	0.107±0.049	-0.035±0.001	0.85	1.91	-0.010±0.003	0.006±0.001	0.64	...
		0.023±0.026	-0.008±0.002	...	...	...	...	...	...	...	...	...	...
	edge-on	0.036±0.052	0.008±0.011	0.51	0.86	0.060±0.012	0.022±0.003	0.94	1.05	0.056±0.008	0.032±0.003	0.92	0.69
		-0.025±0.016	0.004±0.015	...	...	-0.075±0.011	0.025±0.004	...	...	-0.014±0.008	0.021±0.003	...	...
10.5 < logM <sub>*</sub> < 11.0	face-on	-0.032±0.011	-0.006±0.003	0.70	1.27	0.020±0.015	0.009±0.004	0.54	0.87	0.025±0.008	0.017±0.004	0.72	0.74
		0.034±0.029	-0.013±0.004	...	...	-0.027±0.023	0.006±0.004	...	...	-0.030±0.010	0.010±0.004	...	...
	edge-on	0.076±0.030	0.031±0.009	0.75	0.86	0.062±0.006	0.030±0.001	0.97	0.94	0.097±0.006	0.054±0.002	0.98	0.76
		-0.071±0.021	0.022±0.005	...	...	-0.068±0.009	0.027±0.001	...	...	-0.064±0.008	0.036±0.003	...	...

\*  $\tilde{R} = R/R_{SMA}$